VISIBLE PHOTON EMISSION FROM DEFECTS IN HEXAGONAL BORON NITRIDE FLAKES

A Thesis Submitted to
the Graduate School of Engineering and Sciences of
İzmir Institute of Technology
in Partial Fulfillment of the Requirements for the Degree of

MASTER OF SCIENCE

in Physics

by
Volkan FIRAT

January 2017
İZMİR

We approve the thesis of **Volkan FIRAT**

Assoc. Prof. Dr. Serkan ATEŞ
Department of Physics, İzmir Institute of Technology

Assoc. Prof. Dr. Özgür ÇAKIR
Department of Physics, İzmir Institute of Technology

Assoc. Prof. Dr. Mehmet Ertuğrul SOLMAZ
Department of Electrical and Electronics Engineering, İzmir Katip Celebi University

9 January 2017

Prof. Dr. Tuğrul SENGER
Head of the Department of
Department of Physics

Prof. Dr. Bilge KARAÇALI
Dean of the Graduate School of
Engineering and Sciences

ACKNOWLEDGMENTS

Firstly, I thank my advisor Assoc. Prof. Dr. Serkan ATEŞ for his support, understanding and guidance. I appreciate his knowledge. I learned a lot from him.

I also thank Assoc. Prof. Dr. Yusuf SELAMET for his material and laboratory support that made this work possible.

I greatly appreciate Assoc. Prof. Dr. A. Devrim GÜÇLÜ for help with tight binding theory.

I want to thank my thesis committee: Assoc. Prof. Dr. Özgür ÇAKIR and Assoc. Prof. Dr. Mehmet Ertuğrul SOLMAZ.

Thanks to Nahit POLAT, Ozan ARI and Hürriyet YÜCE for their helps, supports and sharing their knowledge.

ABSTRACT

VISIBLE PHOTON EMISSION FROM DEFECTS IN HEXAGONAL BORON NITRIDE FLAKES

Color centers in wide bandgap crystals create discrete energy levels in the bandgap. These discrete energy levels can be used for single photon generation for quantum optics and quantum information applications.

In this work, we created optically active defects in multilayer hexagonal boron nitride (hBN) flakes by annealing technique. We produced seven samples at different annealing temperatures (500°C, 750°C and 850°C) and two non-annealed samples for comparison.

hBN can host defects emitting at visible wavelengths because of its wide bandgap. We made micro-photoluminescence maps to find point defects in the hBN flakes and then carried out power dependent, polarization dependent and temperature dependent measurements to characterize the emissions. We observed highly localized point-like emitters with a size of about 0.5 μm that reach saturation at relatively low excitation powers, show dipole characteristics, have very narrow zero-phonon lines having widths as small as 0.8 meV. These results prove the presence of optically active defects with discrete energy levels.

ÖZET

HEKZAGONAL BOR NİTRÜR PULLARINDAKİ KUSURLARDAN GÖRÜNÜR FOTON IŞIMASI

Geniş band aralığına sahip kristallerde bulunan renk merkezleri, band aralığı içerisinde kesikli enerji seviyeleri oluşturur. Bir çok kuantum optik ve kuantum bilgi uygulamaları için gerekli olan tek-fotonlar bu kesikli enerji seviyeleri kullanılarak elde edilebilir.

Bu çalışmada, çok katmalı hekzagonal bor nitrür (hBN) pulları içinde, tavlama tekniği kullanılarak optik-aktif kusurlar oluşturuldu. Farklı tavlama sıcaklıklarında (500, 750 ve 850°C) yedi örnek ve kıyaslama için iki tavlanmamış örnek hazırlandı.

hBN geniş band aralığı sayesinde görünür bölgede ışıma yapan kusurları barındırabilir. hBN pulları içerisindeki noktasal kusurları bulmak için mikro-fotolüminesans haritalama yapıldı. Daha sonra uyarma gücüne, polarizasyona ve sıcaklığa bağlı ölçümler yapıldı. Ölçümler sonucunda kusurların ortalama 0.5 μm boyutlarında olduğu, göreceli olarak düşük uyarma güçlerinde doyuma ulaştıkları, dipole özellik gösterdikleri, 0.8 meV kadar dar genişlikte sıfır-fonon çizgisine sahip oldukları gözlemlendi. Bu sonuçlar kesikli enerji seviyelerine sahip, optik-aktif kusurların oluştuğunu göstermektedir.

TABLE OF CONTENTS

LIST OF FIGURES

Figure **Page**

LIST OF TABLES

Table **Page**

LIST OF ABBREVIATIONS

ZPL . . . . . Zero Phonon Line
hBN . . . . . Hexagonal Boron Nitride
DFT . . . . . Density Functional Theory
LDA . . . . . Local Density Approximation
GGA . . . . . Generalised Gradient Approximation
DOS . . . . . Density Of States
V_N . . . . . Nitrogen vacancy
PL . . . . . Photoluminescence
BS . . . . . Beamsplitter
NA . . . . . Numerical Aperture
VND . . . . . Variable Neutral Density filter
HBT . . . . . Hanbury Brown and Twiss interferometry
CVD . . . . . Chemical Vapour Deposition
IPA . . . . . Isopropyl Alcohol
DI . . . . . Deionized Water
FWHM . . . . . Full Width at Half Maximum

CHAPTER 1

INTRODUCTION

Today's digital (classical) computers are used heavily for computation, data processing and communication via internet. They use binary data which contains 0 and 1. In the near future this technologies are expected to face some serious problems. For example, the transistors in the processors are almost reach the size limit to function properly because of the quantum tunnelling effect. Another example is the security of communication. Today we mostly use public-key cryptography based on RSA algorithm but it is not 100% secure. RSA can be cracked by algorithms using brute-force and when quantum computers are made it will be more vulnerable. The quantum information technologies can solve these problems. Quantum bits (qubit) are used in quantum information. Qubits can have values 0, 1 and the superposition of 0 and 1 (having both 0 and 1 at the same time). The spin values of electrons can be used as qubits, for example $|up\rangle = 1$, $|down\rangle = 0$ and $\alpha|up\rangle + \beta|down\rangle = superposition$. The polarization of photons can also be used as qubits, for example $0^o = 0$, $90^o = 1$ and $45^o = superposition$.

Generation of polarized, single photons on demand is crucial for the quantum information applications, such as quantum key distribution, linear optics quantum computation, quantum teleportation (Bennett, 1984; Kiraz et al., 2004). Discrete energy levels are the main requirements for the single photon generation. Single atoms and molecules are the first candidates because they have well-known, ready-to-use, stable discrete energy levels. However, working with individual atoms or molecules are very challenging. Therefore, researchers have been trying to find alternative single photon sources for decades. Mostly studied alternatives are quantum dots and color (F) centers in wide bandgap materials (Lounis and Orrit, 2005). Color centers in diamond, zinc oxide (ZnO), silicon carbide (SiC) and recently hexagonal boron nitride (hBN) have been already shown as single photon sources (Aharonovich et al., 2011; Morfa et al., 2012; Lienhard et al., 2016; Tran et al., 2016a).

Our ultimate goal is to create a single photon source for quantum information applications. As a first step, point defects have been generated in multilayer hBN samples by using annealing technique and optical measurements were carried out for optical characterization of the defects.

hBN was preferred because it has several advantages over the other alternatives.

It has a high melting point (about 3000°C), good chemical inertness and mechanical robustness, therefore it can be used in harsh environments (Shi et al., 2010). It has a wide bangap (UV region), it can host optically active defects emitting photons in whole visible and near infra-red region. It can be exfoliated to get atomically thin, 2D layers, so it is suitable for scalable, 2D-hybrid and on-chip devices. Additionally it has been shown that optically active defects in hBN are emitting polarized, single photons at room temperature and they are stable under very high temperatures and in harsh (oxidizing and reducing) environments (Tran et al., 2016b).

CHAPTER 2

LIGHT - MATTER INTERACTIONS

2.1. Spontaneous Emission

Electrons in atoms, molecules and crystals are confined in a potential well. Because of the wave property those electrons can have only certain energy values. These certain energy values are called as energy levels. For example, an electron in a hydrogen atom is confined and has certain, discrete energy levels.

Most of the visible light is produced by a process called spontaneous emission. In this process an electron in the higher energy level decays to a lower energy level spontaneously and during this transition electron emits a photon (radiative transition).

2.1.1. Radiative Transition

Figure 2.1 shows two energy levels for an electron. They are discrete energy levels and the electron can jump between these levels. If the electron, in the ground state, absorbs a photon having energy equals the energy difference between the levels (ΔE) then the electron jumps from the ground state to the excited state (absorption). The electron stays in the excited state for a time (life time) and it turns back to the ground state by emitting a photon with energy equals ΔE.

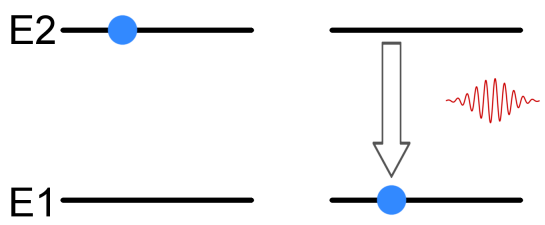

Figure 2.1. Spontaneous emission. The electron in the excited state (E2) decays to the lower state (E1) by emitting a photon.

The transition rate from the excited state to the ground state is given by Equation 2.1

$$\frac{dN_2(t)}{dt} = -A_{21}N_2(t) \tag{2.1}$$

where A_{21} is the Einstein coefficient for spontaneous emission rate and N_2 is the number of atoms in the excited state. Solving this equation for N_2 gives

$$N_2(t) = N_2(0)exp(-A_{21}t) = N_2(0)exp(-t/\tau) \tag{2.2}$$

where $\tau = A_{21}^{-1}$ is the radiative lifetime (Fox, 2006).

2.1.2. Non-Radiative Transition

In solids, the atoms are bonded by Coulomb interactions and they can be modelled roughly as masses attached by springs. The bonded atoms in a periodic lattice structure are quantum harmonic oscillators. They vibrate with certain frequencies and their harmonics. These vibrations are called as phonons. Phonons also have certain, discrete energy levels given in Equation 2.3.

$$E_{phonon} = \hbar\omega\left(n + \frac{1}{2}\right) \tag{2.3}$$

where ω is the phonon mode frequency and n is an integer greater than or equal to 0.

Figure 2.2 shows a diagram contains both the vibrational and electronic energy levels. In this figure, an electron in the ground state is excited by a photon with energy $h\nu$. After some non-radiative transitions (phonon emissions) it reaches the excited electronic state and then spontaneously decays to the ground state by emitting a photon with energy $h\nu'$. The energy difference between the absorbed and emitted photon goes to the phonon modes. The transition mechanism between the ground and excited states involving vibrational modes is explained by the Franck-Condon principle.

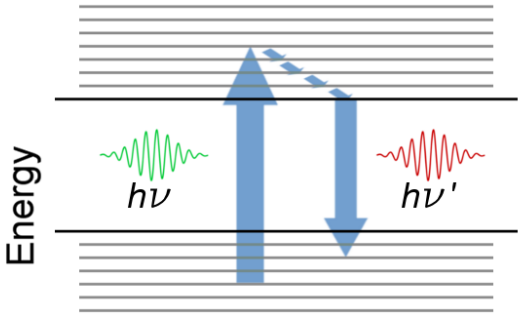

Figure 2.2. Non-radiative transition. An electron in the ground state jumps to a vibrational sublevel in the excited state by absorbing a photon with energy $h\nu$. The electron reaches the excited electronic state by vibrational relaxation (non-radiative transition). Finally the electron decays to the ground state by emitting a photon with energy $h\nu'$ (radiative transition).

2.1.3. Franck-Condon Principle

When an electron goes from one energy level to another the charge distribution changes. Consequently, the force is changed between the ions in the structure. Therefore the positions of the ions must be rearranged according to this new state. This rearrangement changes the electronic levels. However the response of the ions is very slow relative to the transition time of the electron because the mass of the ions is much larger than the electron. For this reason the transition takes place while the system is still in the ground state. After the transition the ions move their new equilibrium positions.

Figure 2.3 shows Franck-Condon diagram. E_0 is the energy state when the electron in the ground state and E_1 is the energy state when the electron is in the excited state. q_{01} is the distance between the equilibrium positions of the ion in E_0 and E_1 states. There are also vibrational energy levels shown as horizontal lines in E_0 and E_1 curves. The black arrow shows a transition from the $n_0 = 0$ vibrational state in E_0 to the $n_1 = 2$ vibrational state in E_1. This transition is called as *vertical* and this is the most probable transition in this condition. After the transition the ion starts to vibrate with a frequency corresponding to $n_1 = 2$ state.

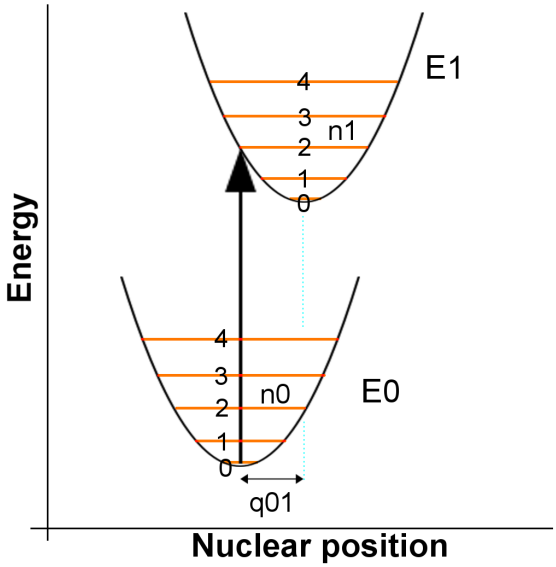

Figure 2.3. Franck-Condon diagram.

The other transitions between the vibrational states are also possible. The transition probability is related with the overlap integral which is given in Equation 2.4

$$S(n_0, n_1) = \int \psi^*_{n_0}(\mathbf{R})\psi_{n_1}(\mathbf{R})d\tau_n \tag{2.4}$$

where ψ_{n_0} and ψ_{n_1} are phonon wavefunctions for ground state and excited state respectively. The intensity of the PL signals from transitions is proportional to the Franck-Condon factor which is given by $|S(n_0, n_1)|^2$.

The PL signal generated by the transitions from $n_1 = 0$ to $n_0 = 0$ states is called as zero-phonon line (ZPL) which is purely electronic transition. At cryogenic temperatures the probability of this transition increases and, therefore the intensity of the ZPL increases. The transitions involving the vibrational states create phonon side bands and they are more visible at higher temperatures (Atkins and Friedman, 2011; Santori et al., 2010).

2.2. Bandgap

Because of the large number of atoms in the bulk materials their energy levels create almost continuous bands. For insulators and semiconductors there are two main bands separated from each other by an energy gap of size in eV scale. One of the band is called as valance band which is filled with electrons, and the other band is called as

the conduction band which is empty when the system is in the ground state. The band gap corresponds to the energy difference between the minimum value of the conduction band and the maximum value of the valance band. If an electron has enough energy than it jumps to the conduction band, and an electron in the conduction band decays to the valance band by emitting a photon. Figure 2.4 shows two examples of energy band diagram in k-space. The electronic transitions are different for these two structures. In the first case as shown in Figure 2.4 (left) the transition is direct and in the second case as shown in Figure 2.4 (right) it is indirect.

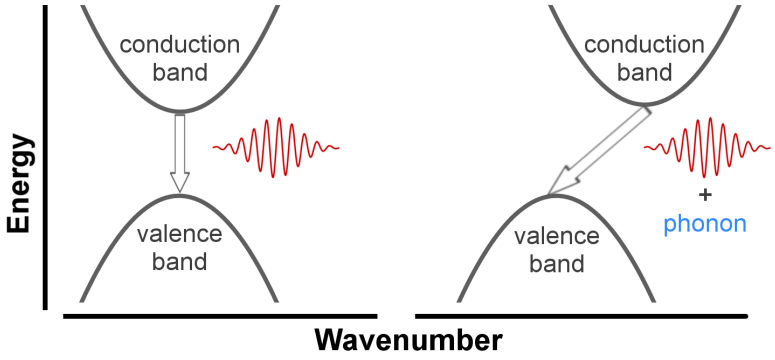

Figure 2.4. (left) Direct and (right) indirect bandgaps.

In direct transition, the minimum of the conduction band is directly above the maximum of the valance band. The value of the wavenumber (k) does not change in the transition between these two points. Therefore the momentum of the electron does not change.

In indirect transition, the minimum of the conduction band and the maximum of the valance band don't have the same k value. The wavenumber and, therefore, momentum of the electron change in this transition. To maintain the momentum conservation the electron also emits phonons in addition to the photon. Indirect transitions are phonon assisted transitions.

2.3. Polarization

Classically the light is electromagnetic wave. It has electric and magnetic field components that are inducing each other while the light propagates. The polarization is defined as the direction of the electric field component. If the light has a certain polarization and it does not change then it is called as linearly polarized. If the light is composed of randomly oriented polarizations then it is called as unpolarized light. In some cases the direction of the polarization is changing as the light propagates. If the polarization rotates in clockwise direction relative to the observer then it is called as right circularly polarized, if it rotates in counterclockwise direction then it is left circularly polarized. If both the direction and amplitude of the electric field component changes then the light is called as elliptically polarized. Mathematically, the electric component of a light propagating in the **k** direction can be defined in the most general form as in Equation 2.5

$$\mathbf{E}_{(\mathbf{x},t)} = (E_1\boldsymbol{\epsilon}_1 + E_2\boldsymbol{\epsilon}_2)e^{i\mathbf{k}\cdot\mathbf{x}-i\omega t} \tag{2.5}$$

In Equation 2.5 $\mathbf{E}_{(\mathbf{x},t)}$ is defined as the combination of two electric fields with magnitudes of E_1 and E_2 and directions of (polarization vectors) $\boldsymbol{\epsilon}_1$ and $\boldsymbol{\epsilon}_2$. All types of the polarizations described above can be written by using this equation (Jackson, 1999).

The interaction Hamiltonian between light and an electric dipole is given in Equation 2.6

$$H = -\mathbf{p}\cdot\mathbf{E}_{(\mathbf{x},t)} \tag{2.6}$$

where **p** is the electric dipole vector and $\mathbf{E}_{(\mathbf{x},t)}$ is the electric field component of the light. The dot product says that the interaction probability, in quantum mechanical sense, depends on the angle between the polarization and electric dipole vector (Fox, 2006).

2.4. Spectral Lineshape

The spectral lineshape function is given in Equation 2.7

$$g(\omega) = \frac{\Delta\omega}{2\pi}\frac{1}{(\omega-\omega_0)^2 + (\Delta\omega/2)^2} \tag{2.7}$$

which has a Lorentzian profile with center at ω_0 and full width at half maximum (FWHM), $\Delta\omega$.

According to the energy-time uncertainty for $\Delta t = \tau$

$$\tau \Delta E \gtrsim \hbar \tag{2.8}$$

and $\Delta\omega$ (FWHM) is

$$\Delta\omega = \frac{\Delta E}{\hbar} \gtrsim \frac{1}{\tau} \tag{2.9}$$

This broadening is called natural (radiative) broadening.

In solids, non-radiative transitions also affect the lineshape. In this case, the spontaneous emission rate equation is redefined as

$$\frac{dN_2(t)}{dt} = -A_{21}N_2(t) - \frac{N_2(t)}{\tau_{NR}} \tag{2.10}$$

where τ_{NR} is non-radiative lifetime. This equation gives the lifetime as

$$\frac{1}{\tau} = A_{21} + \frac{1}{\tau_{NR}} \tag{2.11}$$

which is shorter than the previous lifetime. Again, according to the energy-time uncertainty relation, the lineshape will be more broader. In solids, the non-radiative transitions are very fast relative to the radiative transitions, therefore it has a considerable effect on the FWHM. This mechanism causes a homogeneous broadening (Fox, 2006).

CHAPTER 3

SIMULATION RESULTS

3.1. hBN Crystal Structure

Hexagonal Boron Nitride (hBN) has hexagonal lattice structure consisting of 2D, planar, van der Waals bonded layers similar to graphene with AA' stacking order. In this AA' stacking the positions of boron and nitrogen atoms are alternating in each successive layer as shown in Figure 3.1. The layers in the bulk hBN are weakly bounded by out-of-plane π bonds and can easily be separated as monolayers. Boron and nitrogen atoms are sp2 hybridized in hBN and form 120 degree, planar σ bonds. Because of sp2 hybridization, the monolayer hBN has honeycomb lattice structure like graphene. The lattice constants have been found as $a \approx 2.5$ Å, $c \approx 6.66$ Å, hence the c/a ratio is $c/a \approx 2.66$. The in-plane B-N bond length have been found as ~ 1.45 Å (Warner et al., 2010; Paszkowicz et al., 2002). Theoretically calculated values are as follows; a is between 2.28 and 2.53 Å, and c/a is between 2.37 and 3.68 depending on the stacking order and theoretical model used (Ooi et al., 2006; Topsakal et al., 2009).

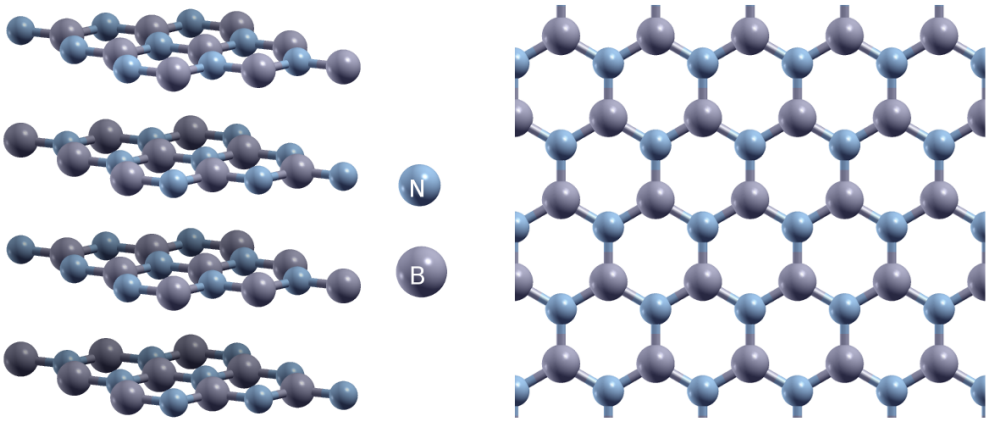

Figure 3.1. Bulk hBN has hexagonal lattice structure consisting of 2D, planar layers (left). The monolayer hBN has 2D, honeycomb lattice structure (right).

In this thesis Quantum ESPRESSO simulation package was used to calculate energy bands, density of states (DOS), phonon bands etc. and XCrySDen software was used to visualize input/output files of Quantum ESPRESSO such as crystal structures and electron density (Giannozzi et al., 2009; Kokalj, 2003). Structural optimization of bulk hBN was carried out with the initial values of $a = 2.50$ Å and $c/a = 2.66$ by using pseudo-potentials based on LDA method and Perdew-Zunger exchange-correlation functional with norm-conservative, scalar relativistic properties which are listed as B.pz-vbc.UPF and N.pz-vbc.UPF in www.quantum-espresso.org. After optimization the crystal structure became smaller and the new values were found as: $a = 2.47$ Å and $c/a = 2.37$. These parameters, method and pseudo-potentials were used in all of our DFT simulations in the following sections.

3.2. Electronic, Optical and Vibrational Properties of hBN

Hexagonal boron nitride is a wide bandgap material but the electronic band structure is still in debate. In literature, several bandgap values are found from 3.6 to 7.1 eV (Topsakal et al., 2009; Ooi et al., 2005; Blase et al., 1995; Zunger et al., 1976; Solozhenko et al., 2001). Also, Watanabe et al. (2004) says that hBN has a direct bandgap, on the other hand Cassabois et al. (2016) says it has an indirect bandgap.

Figure 3.2 (a) shows the unit cell of bulk hBN. It contains two boron and two nitrogen atoms. Figure 3.2 (b) shows its reciprocal lattice and Γ-K-M-Γ path and Figure 3.2 (c) shows the results of our DFT simulation for the electronic band structure of bulk hBN. The calculated value of the bandgap is $E_g = 3.93$ eV and it is indirect. This value is in agreement with the experimental results of Solozhenko et al. (2001) who used laser-induced fluorescence measurement technique and found the bandgap as $E_g = 4.02 \pm 0.01$ eV.

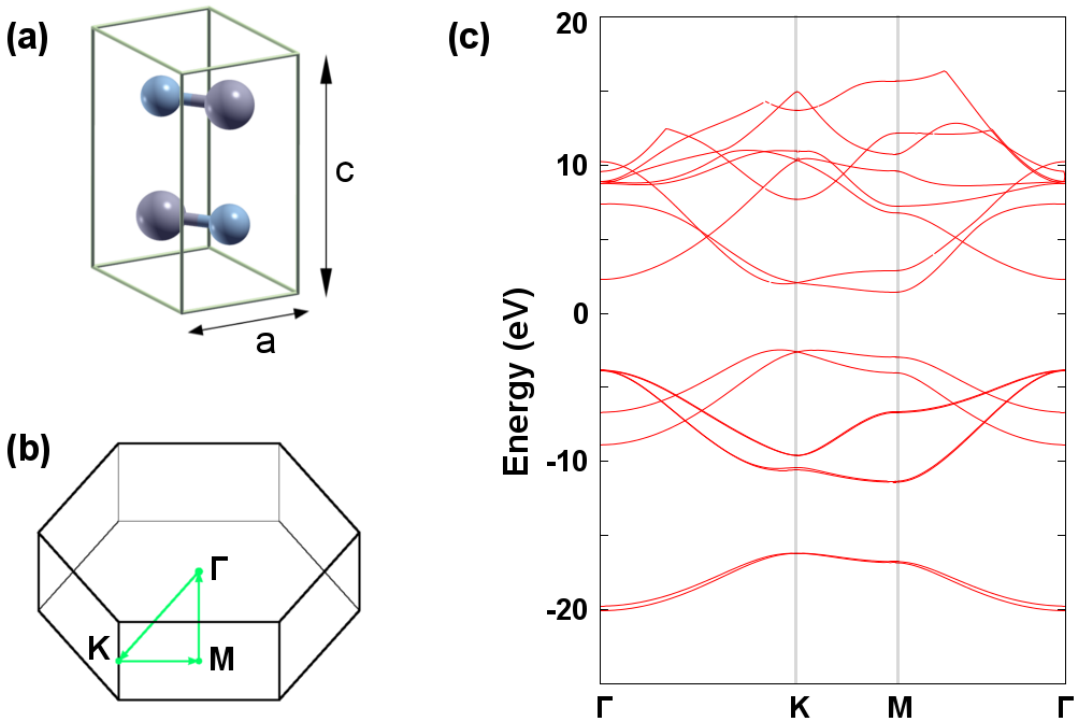

Figure 3.2. DFT simulation results for electronic band structure. (a) unit cell of bulk hBN. (b) reciprocal lattice and Γ-K-M-Γ path. (c) electronic band structure.

As in the case of graphene, the layers of hBN can also be exfoliated easily to get monolayer hBN. The electronic and optical properties of monolayer materials can be different than their bulk forms because of the confinement and unbonded out-of-plane orbitals. Figure 3.3 shows the energy band structure and energy DOS of the monolayer hBN. The nearby but distinct bands in the bulk form become degenerated and the bandgap becomes $E_g = 4.52$ eV which is larger than the bulk's bandgap. There is no experimental result for the bandgap of monolayer hBN currently but our results are comparable with the up to date theoretical study of Topsakal et al. (2009) who found the bandgap as $E_g = 4.64$ eV .

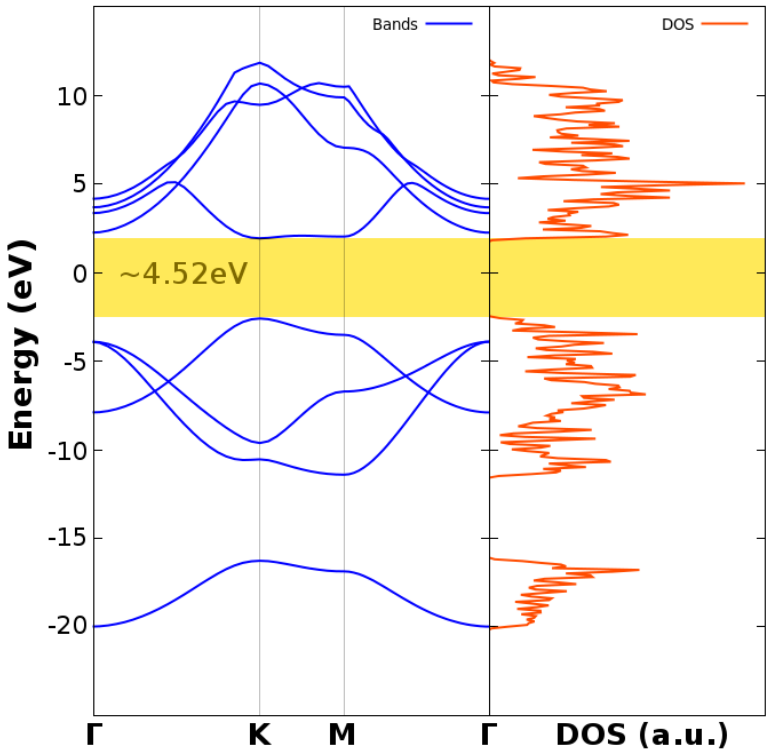

Figure 3.3. DFT simulation results of monolayer hBN. Electronic band structure (left), electronic DOS (right).

The in-plane B-N bonds in hBN are covalent bonds but because of the electronegativity difference between B and N atoms the bonds show ionic character. This tendency effectively determines the optical and electronic properties of hBN. Figure 3.4 is our simulation result that shows the electron density distribution on a plane parallel to the monolayer hBN. The plane was placed a little above the monolayer to produce a smooth distribution map. The electron density increases from dark to light regions. As seen in the figure the electron density is concentrated around the nitrogen atoms. Electronegativity of nitrogen and boron are 3.04 and 2.04 respectively in Pauling scale. The greater electronegativity means that electrons are more attracted.

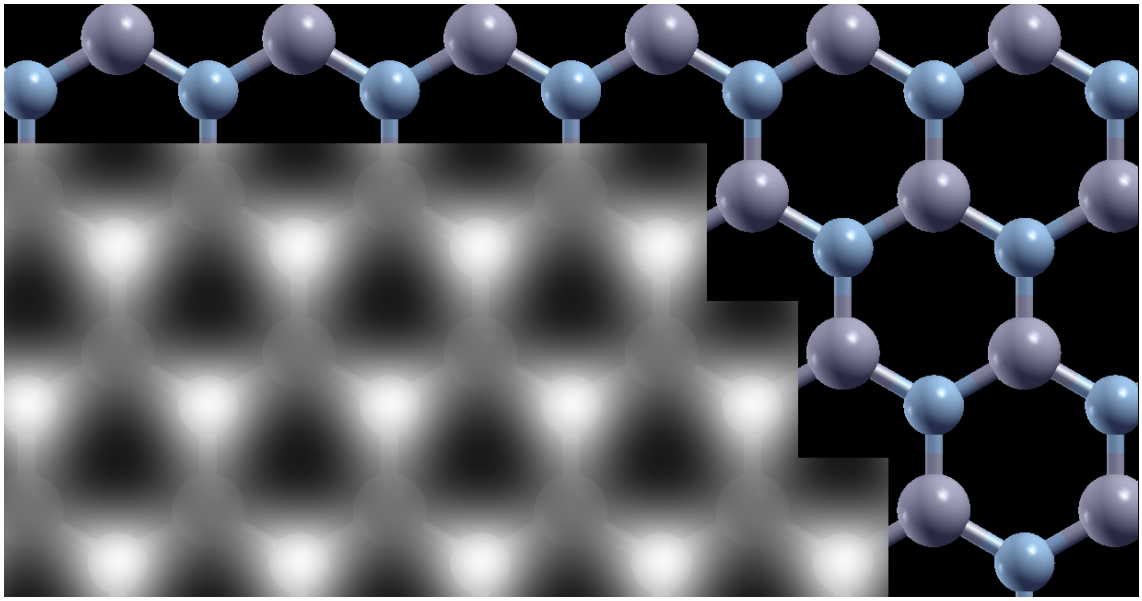

Figure 3.4. Electron density distribution of monolayer hBN.

Vibrations of the ions in a periodic lattice depend on the masses of ions, lattice geometry, lattice constants, valance orbitals, etc. These lattice vibrations are quantum harmonic oscillators and they are called phonons. The phonon frequencies, band structures and DOS can be calculated using the harmonic oscillator Hamiltonian. (Marder, 2010).

Theoretical studies show that the vibrational mode E_{2g} at Γ point has a value of 1363.9 - 1379.2 cm^{-1} and experimentally it is found between 1365.6 - 1370.3 cm^{-1} (Serrano et al., 2007; Lin et al., 2014).

Figure 3.5 shows our simulation results for phonon bands (left) and DOS (right) for monolayer hBN. The frequency of TO branch at the Γ point is 1327 cm^{-1} which is lower than the values in literature.

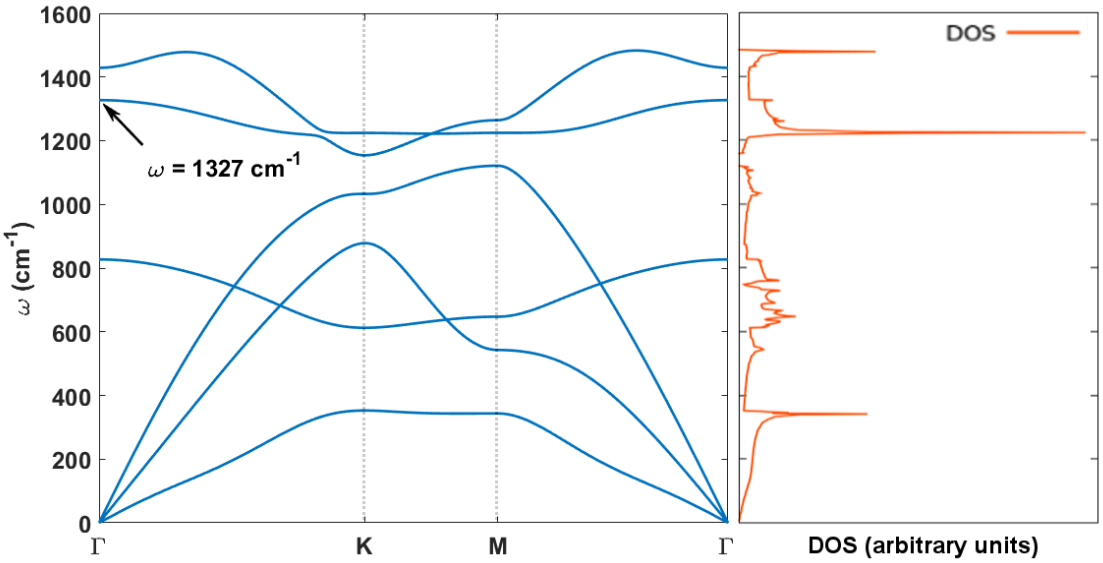

Figure 3.5. Phonon bands (left) and DOS (right) of monolayer hBN.

3.3. Defects in Monolayer hBN

Quantum information applications mostly need single photons. To create single photons one needs discrete energy levels like single atoms have. Isolating and handling a single atom in practice is very challenging. Fortunately, there are many ways to create discrete energy levels such as using quantum dots and point defects (Lounis and Orrit, 2005). It is shown that a point defect in a wide bandgap material can create discrete energy levels and generate single photons (Tran et al., 2016b; Lienhard et al., 2016; Morfa et al., 2012; Choi et al., 2014; Aharonovich et al., 2011).

To show the discrete energy levels formation due to defects in hBN we made a DFT simulation for nitrogen vacancy (V_N). In this simulation 7x7 supercell was produced and a nitrogen atom was removed near the geometric center of the supercell. In final configuration the system has 97 atoms, 49 of them are boron and remaining 48 are nitrogen as shown in Figure 3.6 (left). The Gaussian smearing with a value of 0.02 was applied and local-TF (local density dependent Thomas-Fermi screening which is recommended for highly inhomogeneous systems) was used for mixing-mode. Then the atoms around the vacancy were defined as free-to-move, the others were defined as fixed and left the system to relax. After the relaxation, we observed that the free-to-move atoms moved toward the vacancy center. This final, relaxed configuration was used to calculate the energy bands and the result is shown in Figure 3.6 (right).

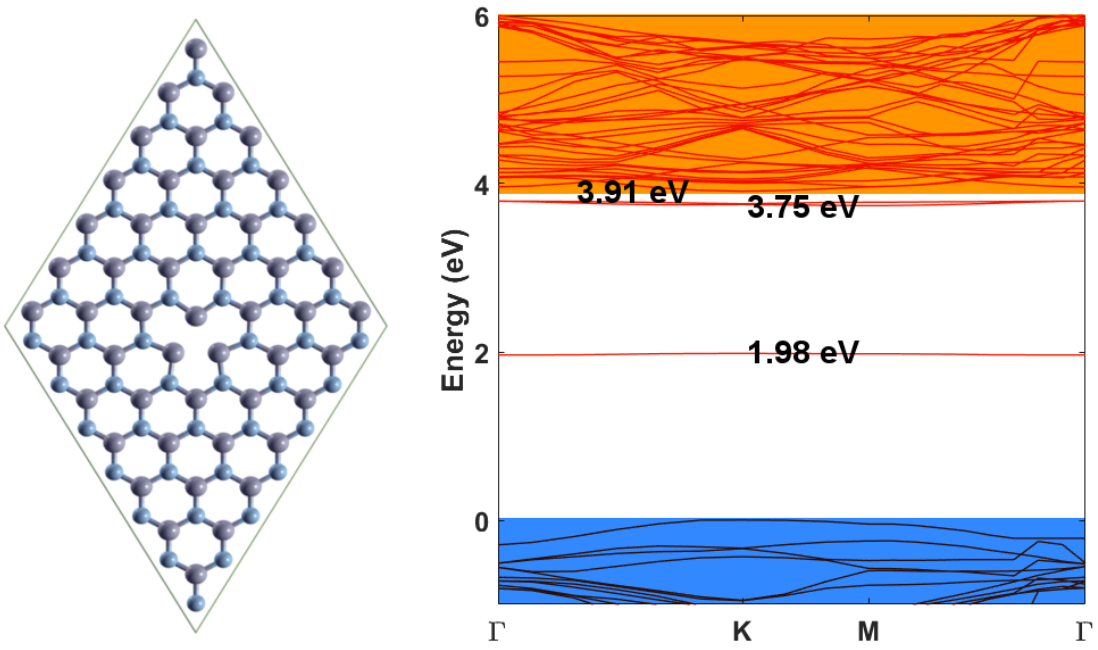

Figure 3.6. Nitrogen vacancy (V_N) defect in 7x7 supercell of monolayer hBN (left). Electronic bands of the structure. Blue region is valance band, orange region is conduction band and red curves are discrete levels in the bandgap of hBN.

As seen in Figure 3.6 (right) V_N defect creates discrete energy levels in the bandgap of hBN. The transitions from 3.91 or 3.75 eV level to 1.98 eV level produce visible photons.

CHAPTER 4

EXPERIMENTAL RESULTS

4.1. Micro Raman/PL Setup

We used the micro Raman/Photoluminescence (PL) setup, shown in Figure 4.1, for all Raman shift measurements and optical characterizations in this thesis.

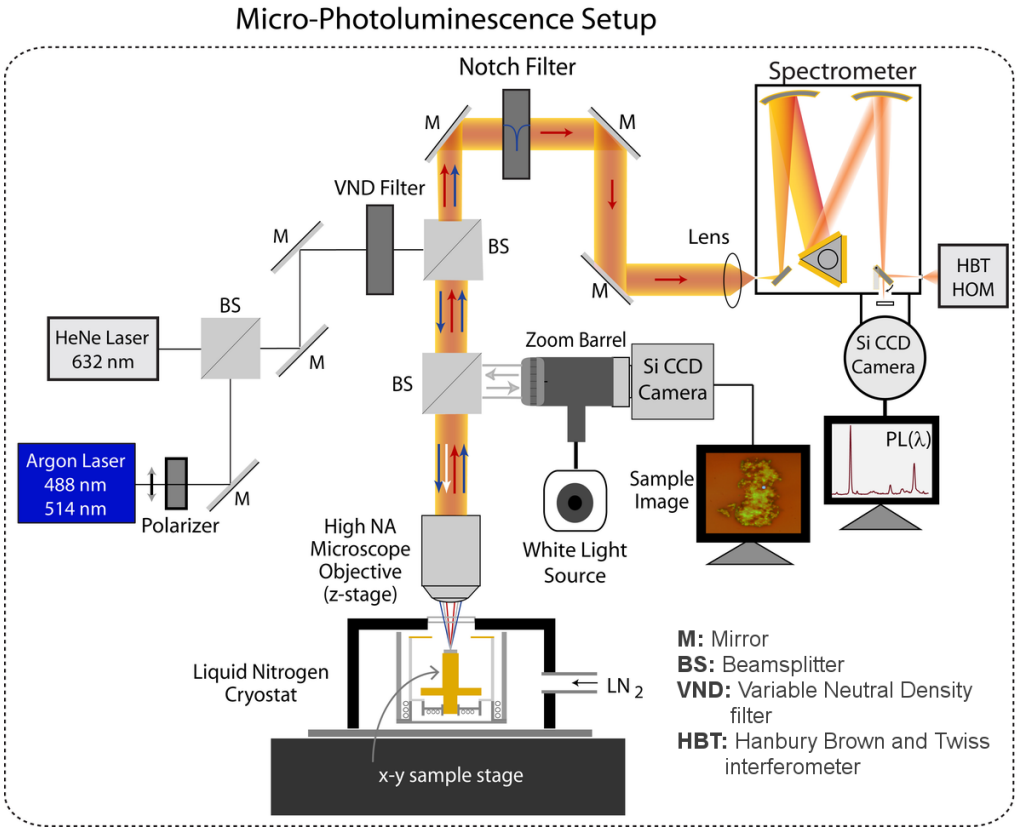

Figure 4.1. Micro Raman/PL setup

The micro Raman/PL setup has two lasers: a HeNe laser, emitting at 632.8 nm and an Argon-ion laser, emitting at multiple wavelengths but only 488 nm and 514 nm were used. The laser is filtered by a narrow-band filter with corresponding wavelength and passing through a half-wave plate which changes the polarization of the light. Then

the laser is guided to the variable neutral-density (VND) filters to adjust the excitation power. By using beam splitters (BS) the laser is directed to a 50x or 100x, high numerical aperture (NA) Olympus microscope objective. The microscope objective focuses the laser on the sample which is mounted on a computer-controlled xy-stage. The scattered/emitted light from the sample is collected by the same objective. The collected light is directed to a Notch filter to block the laser light, therefore only the emitted light can reach the spectrometer having a length of 750 mm and containing 150, 600, 1800 gr/mm gratings. After leaving the spectrometer the light goes to a high-sensitive, cooled (about -70°C) Si CCD sensor. Finally, the spectrum is acquired from the CCD camera and recorded by a computer.

For low-temperature experiments we used Linkam THMS600 stage which has a liquid-nitrogen pump and a resistive heating element to adjust the temperature of the sample stage. The temperature can be fixed in a range from +300°C to –196°C. The Linkam stage operates very shaky because of the liquid-nitrogen pump that affects the mapping process negatively. To fix this problem we made a custom adaptor for the Linkam to mount it to the xy-stage.

The Hanbury Brown and Twiss (HBT) setup for photon-correlation measurements was under construction while this thesis was writing. For this reason there is no photon-correlation result in this work.

4.2. Sample Preparation

A 100ml hBN multilayer flake solution as shown in Figure 4.2 (left) and a CVD (Chemical Vapour Deposition) multilayer hBN on copper foil as shown in Figure 4.2 (right) were ordered from graphene-supermarket.com. The supplier states that the hBN flake solution is an ethanol/water solution containing hBN flakes with a concentration of 5.4 mg/L. The majority of flakes have 1-5 layers. The average size of the flakes is in a range of 50-200 nm. The CVD multilayer hBN was grown on a 2”x1” copper foil. This hBN sample has an average thickness of 13 nm and covers the 90-95% of the copper foil.

We tried Si wafers, SiO_2/Si wafers with 300 nm oxide layer and sapphire wafers as substrates. The SiO_2/Si wafers gave the best optical contrast among them, therefore we chose SiO_2/Si wafers as substrates in our samples.

Figure 4.2. Multilayer hBN flake solution (left) and CVD multilayer hBN on copper (right).

SiO_2/Si wafers were cut to make substrates about 1x1 cm in size. For cleaning process, three beakers containing acetone, Isopropyl alcohol (IPA) and deionized water (DI) were placed in an ultrasonic cleaner. The SiO_2/Si substrates were immersed in acetone and wait 10 minutes then rinsed with acetone before transferring to the next beaker. We repeated the same steps with IPA and DI water in sequence. After the cleaning process, the SiO_2/Si substrates were dried quickly by blowing nitrogen gas to prevent the formation of spots due to the evaporation of water drops.

The sample preparation procedure for the hBN flake solution was as follows. 5-20 μL hBN solution was dropped on a SiO_2/Si substrate. It was allowed to dry in ambient conditions.

The sample preparation procedure for the CVD multilayer hBN was as follows. The copper foil was coated with polymer (photo-resist) and the polymer was cured at 70°C. Then the polymer/Cu was immersed in $FeCl_3$ solution to etch the copper. After the copper was completely etched it was rinsed with DI water. The remaining polymer/hBN was placed on a SiO_2/Si substrate and ensuring that the hBN side of the polymer/hBN faced with the substrate. The sample was heated to 120°C and wait 2 minutes to melt the polymer for adhesion. Then sample was immersed in acetone to dissolve the polymer. The remaining hBN/substrate sample was rinsed with acetone.

To create defects in hBN we used the annealing technique. First the sample was placed in quartz tube furnace and the furnace was heated to 300°C and wait 30 minutes at this temperature for cleaning purpose. After thermal cleaning, the furnace was heated up to the annealing temperature and wait 30 minutes under the 260 sccm Ar flow to prevent oxidation. This annealing process creates defects in hBN. We produced many samples at 500°C, 750°C and 850°C annealing temperatures. We also prepared reference samples, which were not annealed, to investigate the effects of the annealing on the defect type and

compare the results from the annealed and non-annealed samples.

Figure 4.3 shows the optical images of some samples before and after the annealing. As seen in the first row, there are some geometric patterns and some small solid pieces on the sample before annealing. After annealing the geometric patterns disappeared but the solid pieces remained. Most probably, the geometric patterns were contaminations. The remaining pieces are accumulation of hBN flakes as explained in the next section.

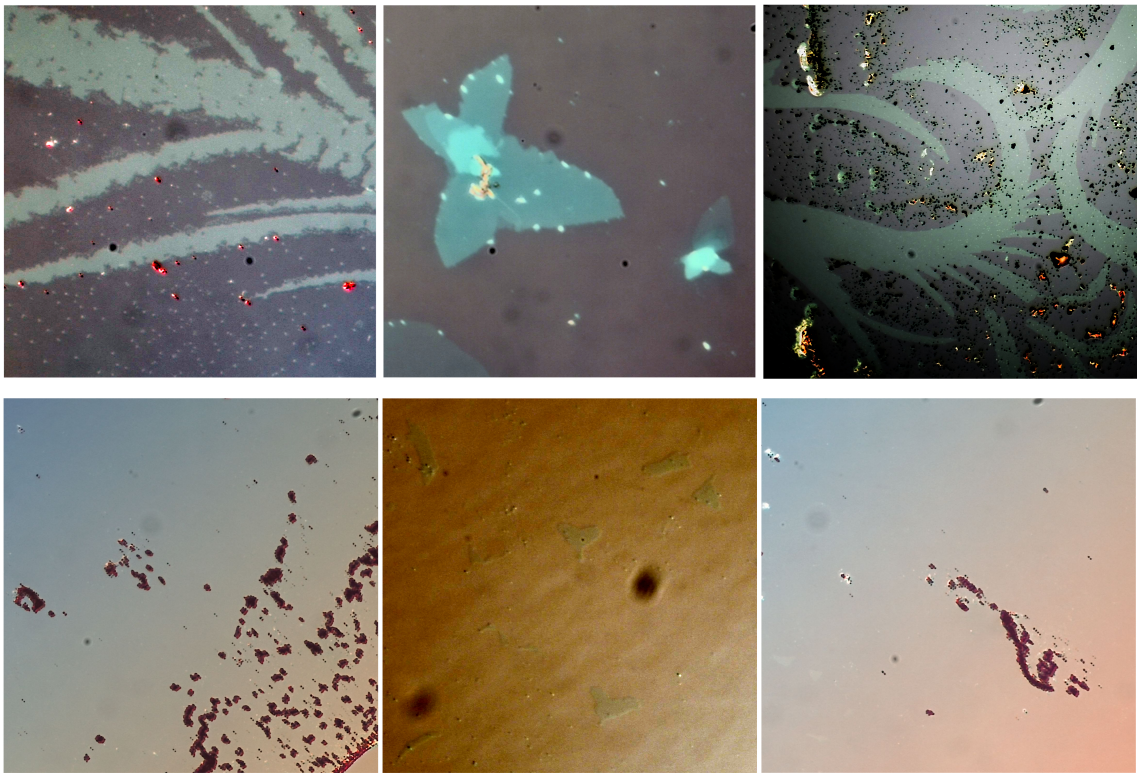

Figure 4.3. Optical images of some samples before (first row) and after (second row) annealing.

4.3. Raman Measurements

Raman spectroscopy measurements on the hBN samples were carried out by using 514.5 and 488 nm laser emissions from the Ar-ion laser. The calibration was done by shifting the Si peak to 520 cm^{-1} (Parker Jr et al., 1967). At room temperature measurements the 100x objective were used and at low-temperature measurements the 50x objective were used because of the limited working distance. Mostly the 600 gr/mm grating was used for Raman measurements because it is able to cover both Si peak and hBN

peak in a single spectrum with a 0.4 cm^{-1} resolution. For detailed analysis the 1800 gr/mm grating was used, for example determining peak position and full width at half maximum (FWHM) value more precisely or obtaining better results for fitting.

In the samples, various flake-like and bulky structures were observed. We got strong Raman peaks around 1365 cm^{-1} from the bulky structures but we couldn't get a Raman peak from the flake-like structures. According to Gorbachev et al. (2011) the intensity of the Raman signal of monolayer hBN is fifty times weaker than the monolayer graphene's. For this reason we concentrated on the bulky structures ('bulk' will be used instead of 'bulky structure' after this point).

A typical Raman spectrum of bulk hBN sample is shown in Figure 4.4. In this measurement 488 nm laser and 600 gr/mm grating were used. The peak between 400-600 cm^{-1} is the Si Raman peak calibrated to 520 cm^{-1} and the other peak between 1200-1400 cm^{-1} is the hBN Raman peak. The Lorentzian fitting gives 1366.3 cm^{-1} for the position and 10.6 cm^{-1} for the FWHM of the hBN Raman peak which are consistent with the results in literature (Gorbachev et al., 2011; Tran et al., 2016b).

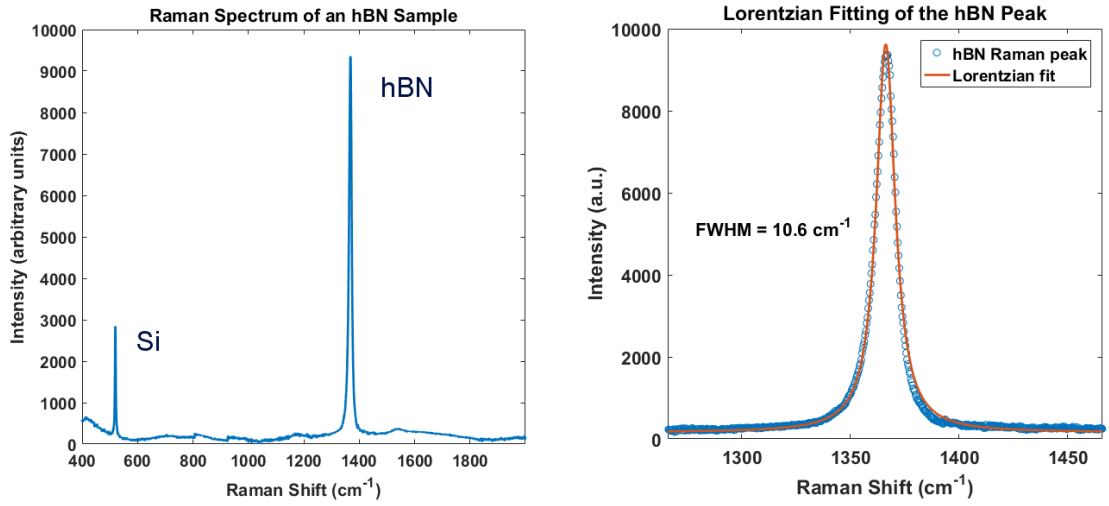

Figure 4.4. Raman measurement of a bulk hBN by using 488 nm laser and 600 gr/mm grating. Raman spectrum covering both Si and hBN Raman peaks (left) and Lorentzian fit applied to the hBN peak (right).

We made a series of Raman measurements on a bulk to see how the intensity is related with the thickness of the structure. In Figure 4.5 it is easily seen that the intensity of the Raman peak of hBN increases with the increasing thickness as expected. The colored dots in the optical image correspond to the Raman measurement points and the spectrum of the each point is shown with the same color of the corresponding dot's.

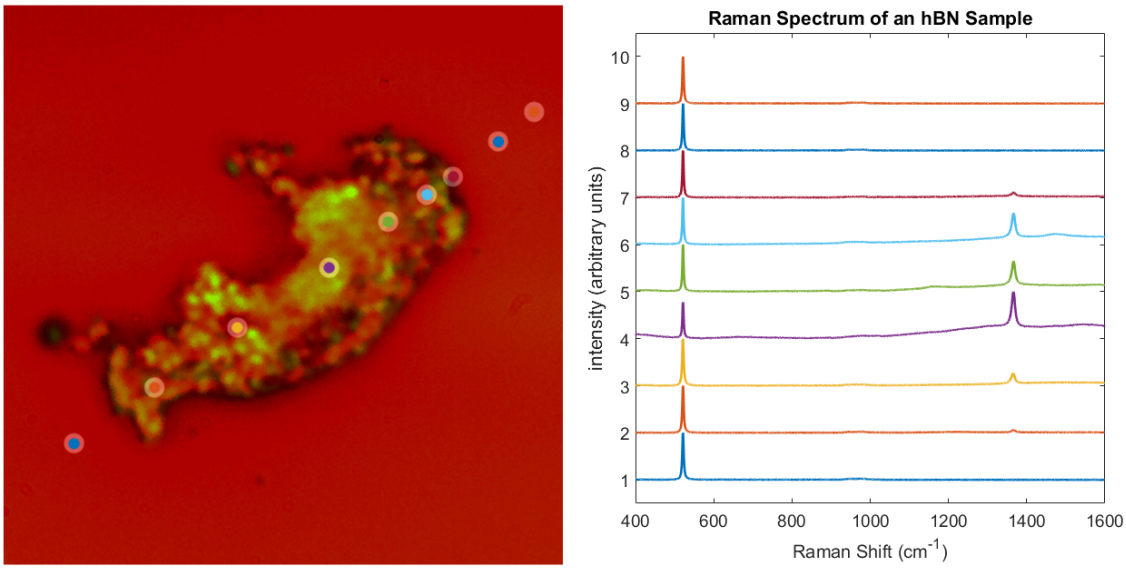

Figure 4.5. Raman measurement series on a bulk. 100x optical image (left), Raman spectra (right).

For detailed view and analysis, micro-Raman mapping technique was used and obtained tens of Raman maps from several bulk samples. Raman maps are able to give details at submicron resolutions and as mentioned earlier the intensity of the Raman signal is proportional with the thickness of the bulk hBN, therefore it is a powerful technique to create high-resolution images showing both distribution and thickness of the hBN samples. In Figure 4.6 100x optical image (left), hBN Raman map (middle) and Si Raman map (right) of a bulk were given.

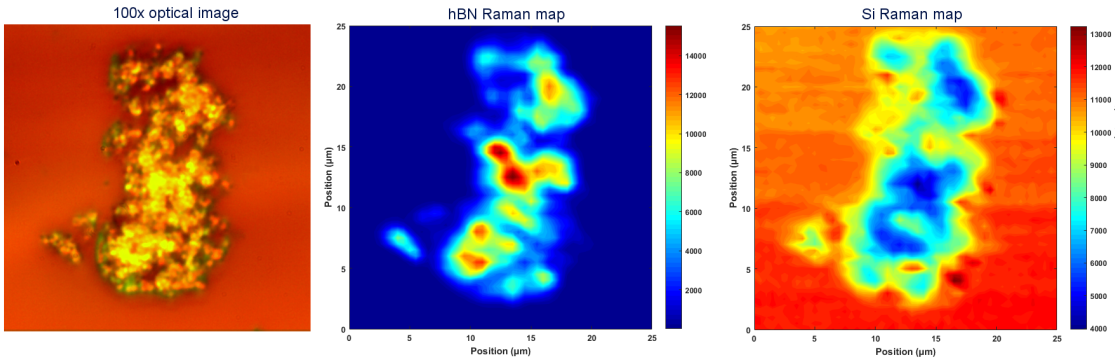

Figure 4.6. 100x optical image (left), micro-Raman map of hBN (middle) and micro-Raman map of Si (right). Intensity increases from dark blue to dark red.

In this micro-Raman map 488 nm laser and 150 gr/mm grating were used. The step size is 0.5 μm and the map size is 25x25 μm. The map data contains 2601 spectra and the corresponding peak frequency for Si or hBN is filtered to generate Raman map. The hBN Raman map was generated by using the intensity values for 1363.9 cm^{-1} and the Si Raman map was generated by using the intensity values for 520.0 cm^{-1}. The Si substrate and hBN sample are clearly distinguished.

4.4. Photo-Luminescence Measurements

When analysing a PL spectrum, it is crucial to identify and differentiate the emissions related with Raman scattering. Using the wavelength of excitation source, λ_0, and Raman shift of the material, ω, the wavelength of Raman scattered photons, λ_R can be calculated easily. For example the Raman shift of Si is 520 cm^{-1} and it corresponds to an emission wavelength of 500.7 nm if 488 nm laser is used. The Raman shift of a material is a constant property and it does not change with the wavelength of the excitation laser. Therefore, if the wavelength of the laser is changed, wavelength of the Raman scattered photons shifts according to $\omega = \lambda_0^{-1} - \lambda_R^{-1}$.

Table 4.1 shows the wavelengths of Raman scatterings for Si and hBN (assuming that it has a Raman signal at 1365 cm^{-1}) using 488.0 nm, 514.5 nm and 632.8 nm excitation wavelengths.

Laser	Si (520 cm^{-1})	hBN (1365 cm^{-1})
488.0 nm	500.7 nm	522.8 nm
514.5 nm	528.6 nm	553.4 nm
632.8 nm	654.3 nm	692.6 nm

Table 4.1. Excitation laser wavelengths and emission wavelengths of the Raman scattered photons of Si and hBN. The Raman shifts of the materials are given in paranthesis.

In Figure 4.7 the spectrum of an hBN sample has been given. As seen in this figure the Raman scattering of Si has shifted while the PL peak near 600 nm has remained fixed. The wavelength of a PL signal depends on the energy difference between the excited and the ground state, therefore it doesn't change with the excitation source's wavelength. The

hBN signal is very weak to be visible in this figure, presumably the source of the PL signal is a defect at the edge of the hBN sample.

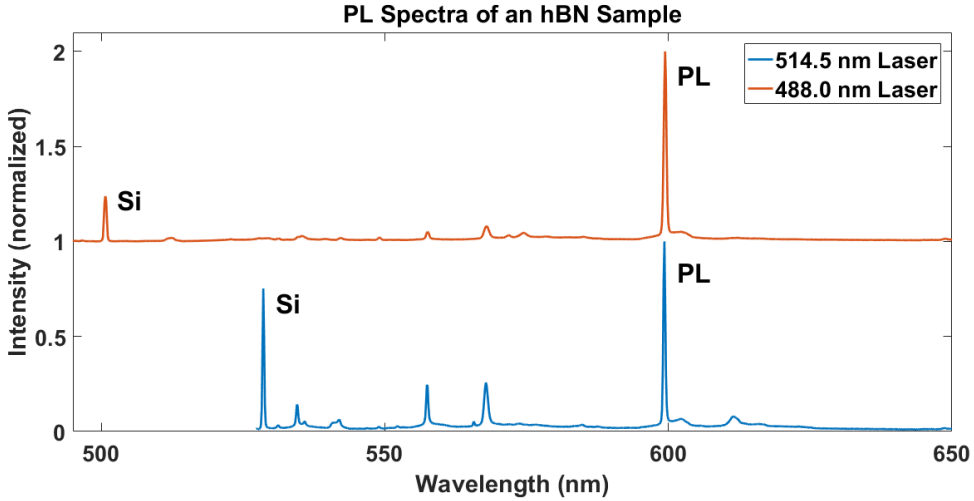

Figure 4.7. Spectra of an hBN sample using 488.0 nm and 514.5 nm excitation lasers. The PL signal remained fixed and the Raman scattering signal of Si shifted.

A point defect can be described as an object in atomic sizes. For this reason finding a defect is not easy. A defect can be found by random walking over the sample while observing the PL spectrum. But this is not a suitable way to locate the defects. Therefore we used micro-PL mapping to find and locate the defects in samples. In this method the sample is scanned point by point in a defined area with a given step-size. We used step-size values as small as 0.1 μm and located the defects very precisely. By means of the micro-PL mapping, the PL spectra of several defects can be analysed by using a single map data and these defects can be found again easily for further characterization.

The point defects are expected to be as small as atoms but the real size can not be determined by optical microscopes. Figure 4.8 shows the PL map of an isolated defect (left) and its horizontal cross section (right). The horizontal axis is the position and the vertical axis is the intensity in the cross section plot. The Gaussian fit was applied to the experimental data and FWHM is found as $0.58\ \mu m$. This is not the real size of the defect, it is limited by the optical resolution of the laser light and grating, focus length and NA of the objective, and the step size of the map. In the PL map x and y axis are the physical positions and the intensity values have been shown by colors in a range between dark blue (relatively the lowest intensity) and dark red (relatively the highest intensity).

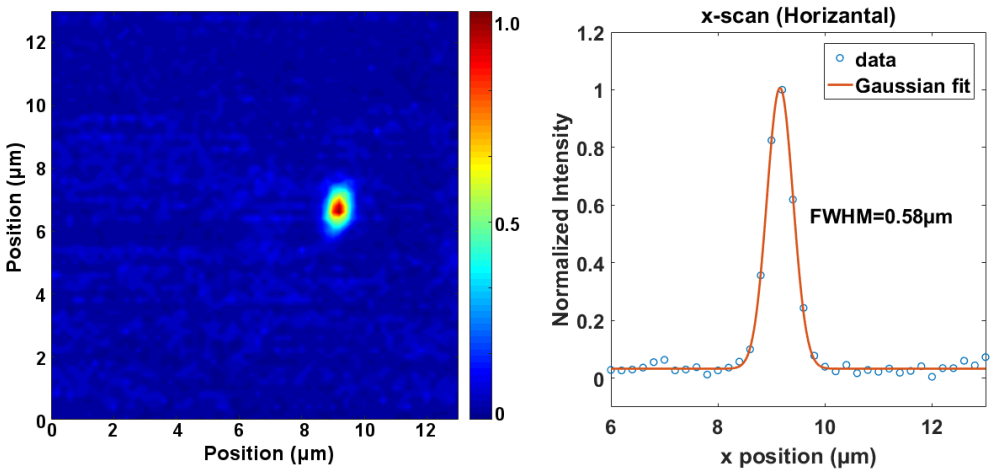

Figure 4.8. A single, isolated defect in hBN (left) and Gaussian fit of horizantal scan passing the defect's center (right).

As mentioned in the previous section, the intensity of the hBN Raman signal is proportional to the thickness of the sample and these regions were shown with reddish colors in the maps. These red regions are usually very crowded with defects and it requires too much work to identify the spectra of individual defects. Figure 4.9 shows regions crowded with defects numbered as 3,4,5 and corresponding spectra. As seen in the figure the spectra of 3,4,5 are superimposed. On the other hand the defects numbered as 1 and 2 are very isolated from the others and their individual spectra are obtained clearly.

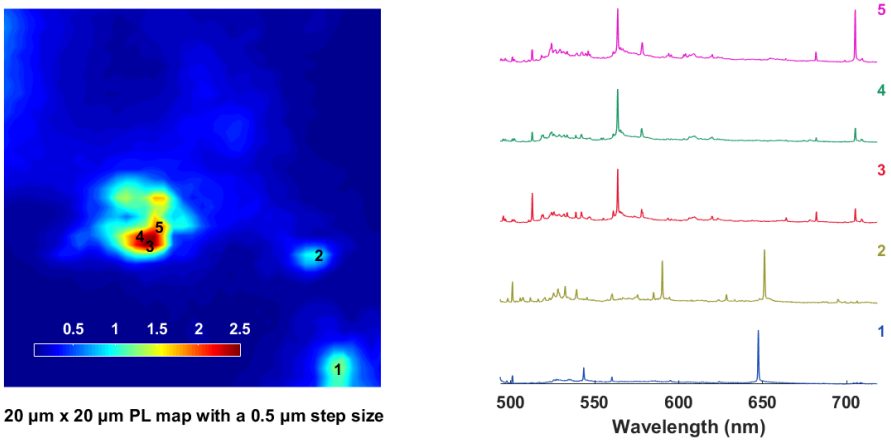

Figure 4.9. PL map of an hBN sample at 150K (left) and spectra of the defects (right).

The isolated defects like 1 and 2 are usually found in the regions corresponding to the bluish regions in the hBN Raman maps. Therefore the hBN Raman maps can be used as a guide to find isolated defects.

Figure 4.10 shows a PL map of an hBN sample (left) and spectra of the some selected emitters (right), most probably hBN defects. This measurement was taken at room temperature by using 100x objective. The size of the map is 25 μm x 25 μm and the step size is 0.5 μm. Hence, it contains 2601 (51 x 51) measurement points. The spectrum of the each point was recorded and then using a Matlab code, all spectra analysed to find unique PL peaks. To generate a PL map, first the intensities of a selected peak's wavelength (in this case we have 2601 intensity values) are placed in a suitable matrix (in this case 51x51 square matrix) then the matrix is plotted using the contourf command in Matlab. To generate a PL map of multiple peaks, first the corresponding matrices were created and filled with the normalized intensity values, then all of the matrices were summed and this final matrix was plotted. The PL map in Figure 4.10 was generated by adding five different matrices. As seen in the PL map, each selected peak has a maximum at different points. It means that there are five different highly localized emitters in this map. The spectrum of the each point (emitter) has been given next to the map. As seen in the figure each point has a distinct spectrum.

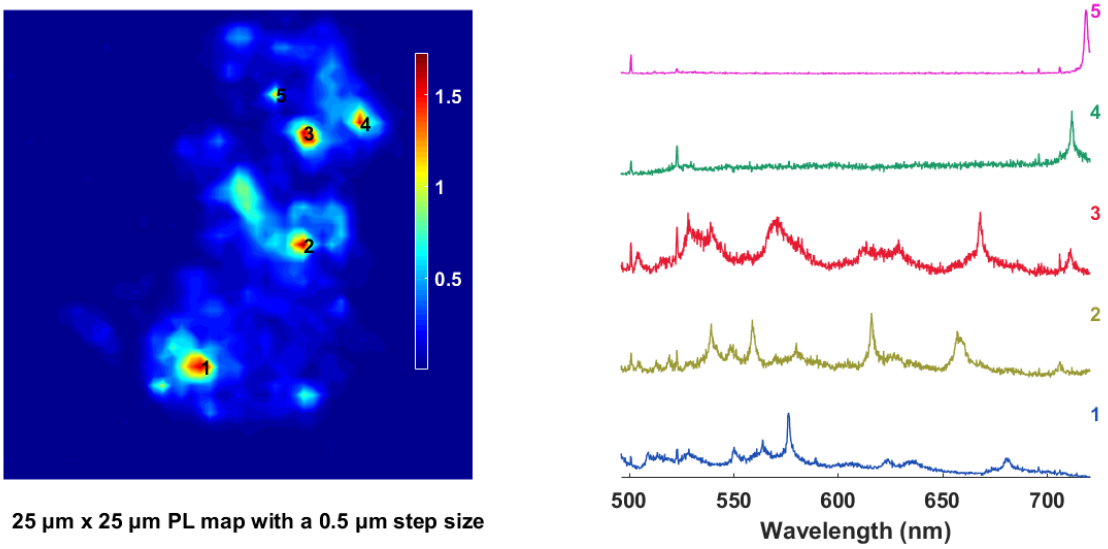

Figure 4.10. PL map of an hBN sample at room temperature (left) and spectra of the selected emitters (right).

4.5. Polarization Measurements

Polarization of light is used in quantum information applications to create qubits. Therefore it is crucial to have a polarized, single photon generator for applications. Excitation polarization dependence of PL spectrum gives information about the dipole properties of the emitter. In this section polarization dependence of PL spectra of the defects has been investigated. The polarization of the Ar-ion laser was changed by using the half-wave plate shown in Figure 4.1 and the PL spectrum was recorded at every 10^o, in critical cases at every 5^o, steps until the polarization made a full turn.

Figure 4.11 (a) shows the PL spectra of a defect at 0^o and 90^o excitation polarizations. The intensity of the peak at 687 nm decreases dramatically at 90^o. Figure 4.11 (b) shows the excitation polarization dependence of the integrated intensity of the peak at 687 nm in polar coordinates. The integrated intensity is the area of the Lorantzian fit applied to PL peak. The blue circles are experimental data and the red plot is the fitting function. As explained in the section 2.3 the light-dipole interaction depends on the angle (θ) between the excitation polarization and the electric dipole moment of the emitter. Theoretically the PL intensity of a dipole is given by

$$I = I_o cos^2(\theta) \tag{4.1}$$

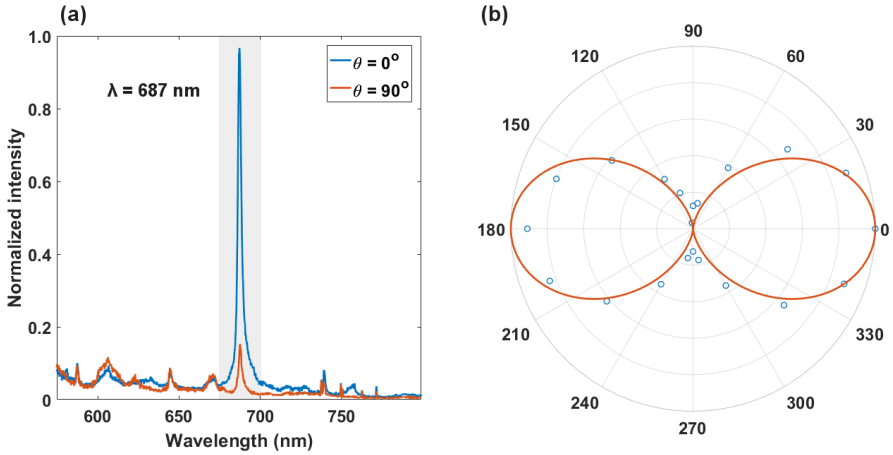

Figure 4.11. Excitation polarization dependence of PL. (a) PL spectra of a defect at 0^o and 90^o excitation polarizations. (b) Excitation polarization dependence of the peak at 687 nm. Blue circles are experimental data and red plot is fitting function. Radial axis is the normalized integrated intensity and the angular axis is the polarization angle.

Visibility value reveals the characteristics of the dipole and it is calculated using the Equation 4.2.

$$V = \frac{I_{max} - I_{min}}{I_{max} + I_{min}} \tag{4.2}$$

The excitation visibility of the 687 nm peak is about 78% for $I_{max} = I_{\theta=0}$ and $I_{min} = I_{\theta=90}$. Theoretically, the visibility reaches to 100% for a single dipole that is perpendicular to the optical axis. Another emitter near the dipole, background emission and the direction of the dipole relative to the optical axis are possible reasons for the lower visibility.

The micro-PL setup does not contain a polarizer for emission polarization measurements. For this reason the emission polarization data is missing. The micro/PL setup will be extended for this measurement.

4.6. Power Dependence Measurements

In this section excitation power dependence of the PL spectra from defects has been investigated to obtain information about the electronic band structures of them. The Ar-ion laser in the Micro-PL setup was used as excitation source and the power was measured just after the VND filter shown in Figure 4.1. The excitation power was measured as 10 mW when the transmission is 100%. The power on the sample was also measured and found as 6.4 mW. The size of the defects are extremely small compared to the laser's spot size and determining the exact power (or power density) on the defects is beyond the capabilities of our setup. Therefore in this section relative excitation power has been taken into account to show the power dependence of the PL spectra.

Figure 4.12 (a) shows the excitation power dependence of a defect's PL intensity at four different power values and as seen in this figure intensity of the PL peak at 605.6 nm increases rapidly from 0.1 mW to 1 mW but there is no remarkable change from 4 mW to 10 mW. On the other hand the background emission continues to increase almost linearly with power. These results show that the PL signal saturates at very low power compared to the background. To exhibit this saturation behaviour, detailed power-dependence measurements were carried out. Figure 4.12 (b) shows the saturation curve of the PL emission at 605.6 nm . The power dependence of hBN Raman scattering is also shown for comparison. Experimental data are shown by blue (PL) and green (Raman) circles and fitting results are shown by red (PL) and violet (Raman) curves. To get these results Lorentzian fit was applied to PL and Raman spectra, and integrated intensities were obtained from fitting. Then the results were normalized for PL series and Raman series independently.

Finally the normalized-integrated intensities are plotted as a function of excitation power. The fitting function, shown in Equation 4.3, is used for PL data and it clearly shows the saturation behaviour.

$$I = I_{\infty} \times \frac{P}{P + P_{sat}} \tag{4.3}$$

In Equation 4.3, I_{∞} is the maximum emission rate, P is the excitation power and P_{sat} is the excitation power at saturation. As seen in Figure 4.12 the PL emission of the defect reaches the saturation at very low excitation power relative to Raman scattering whose intensity increases almost linearly. The fitting function gives $P_{sat} = 1.1$ mW for defect's PL emission. This saturation behaviour at low powers indicates the existence of discrete energy levels.

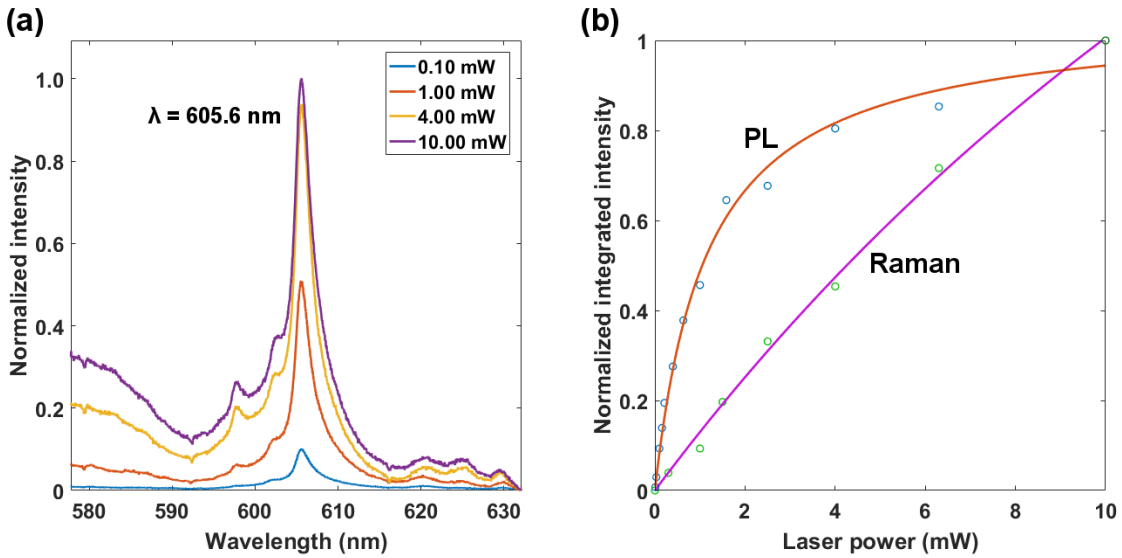

Figure 4.12. Excitation power dependence at room temperature. (a) PL spectra of a defect at different powers. (b) Integrated intensities of the PL emission and hBN Raman scattering as a function of excitation power. The circles show the experimental data and curves show the fitting functions. The laser power is measured after the VND filter shown in Figure 4.1

4.7. Temperature Dependence Measurements

In this section temperature-dependence of intensity, integrated intensity, FWHM and peak center of PL emissions have been investigated. The Ar-ion laser in the micro-Raman/PL setup, shown in Figure 4.1, was used as excitation source emitting at 514.5 nm and 488 nm and the long-working-distance, 50x Olympus objective lens was used to focus the laser and collect the emissions. To control the temperature the Linkam THMS600 temperature-controlled stage was used.

Figure 4.13 shows the temperature-dependence of a PL peak from a point defect in hBN. In this experiment the 600 gr/mm grating was used. The graph at left contains the results at both 293 K (20°C) and 83 K (–190°C) for comparison. The smaller graphs at right show experimental data and fitting curve on each spectrum individually for detailed comparison. The blue circles are experimental data and the red curves are fitting functions.

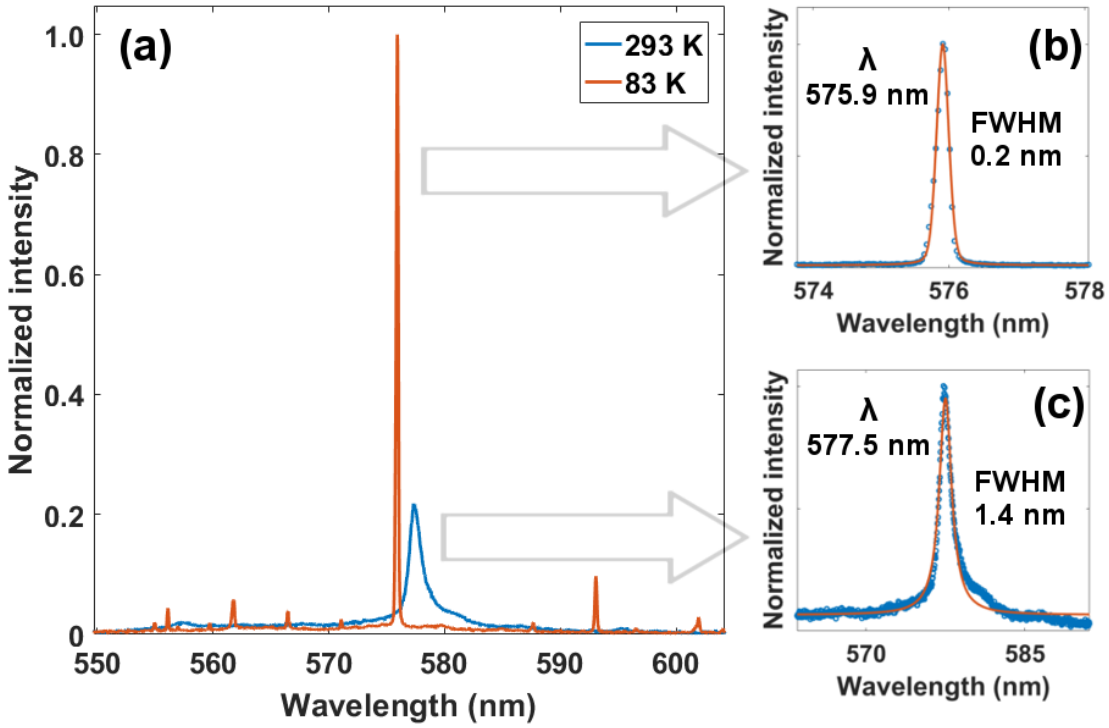

Figure 4.13. Temperature dependence of a PL emission from a defect. (a) PL spectra at 293 K and 83 K. (b) PL peak at 293 K and (c) at 83 K.

The shape of the PL signal is more Lorenztian-like at high temperatures and it is more Gaussian-like at low temperatures. Because of this profile change, pseudo-voigt profile (superposition of Gaussian and Lorentzian functions) was used as fitting function which is given in Equation 4.4

$$y = A(\alpha \frac{2}{\pi} \frac{w}{4(x - x_c)^2 + w^2} + (1 - \alpha) \frac{\sqrt{4ln(2)}}{w\sqrt{\pi}} exp(-4ln(2) \frac{(x - x_c)^2}{w^2})) + y_o \quad (4.4)$$

where A is area, w is full-width at half maximum (FWHM) and x_c is peak center. The values obtained from the fitting are given in Table 4.2. As seen in the table the peak center shifts from 577.5 nm to 575.9 nm and it corresponds to a blue-shift about 1.6 nm or about 6 meV. The FWHM is 1.42 nm (about 5.3 meV) at 293 K and 0.21 nm (about 0.8 meV) at 83 K but the latter value is limited by the resolution of the grating. The peak intensity increases while the temperature is decreasing. As a result the PL signal is getting higher and narrower, and the peak center is shifting to higher energies as temperature decreases. As explained in section 2.1.3 the intensity of ZPL signal is increased and it is getting narrower because the ZPL transition is more probable at low temperatures. The peak center shifts to higher energies as the temperature decreases because the lattice is getting smaller (Jungwirth et al., 2016).

Temperature (K)	Peak center (nm)	FWHM (nm)	Peak height (a.u.)
293	577.5	1.42	1660
83	575.9	0.21	8575

Table 4.2. The evolution of a PL signal with temperature. The values obtained from the fitting function given in Equation 4.4 applied to the experimental data.

4.8. Statistics

Figure 4.14 shows the histogram of the PL peaks. This histogram is obtained by using 13 PL maps which are most suitable ones for this statistics, others are not suitable because they do not cover the wavelength range of this histogram completely or they

have very noisy spectra. The horizontal axis is the wavelength covering a range of 490-720 nm, and the vertical axis is the number of peaks. Each bar has a width of 10 nm. As seen in the histogram 520 and 530 nm bars are the highest ones. Most probably these emissions come from the same kind of defects but because of the strains, sample-substrate interactions, resolution of the grating and some other reasons the peak positions changed slightly.

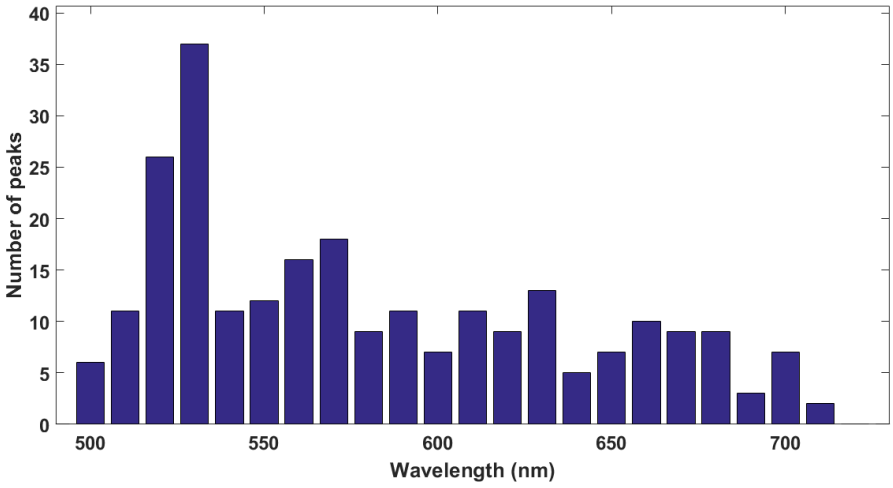

Figure 4.14. Statistics of the PL peaks.

Figure 4.15 shows the histogram of the PL peaks from annealed and non-annealed samples for comparison. The wavelengths around 520 and 530 nm have the highest population in all samples. The samples annealed at 500°C and 750°C have 89 and 72 peaks respectively. First one has a more uniform distribution. Also, in the first one there is an accumulation between 600 and 650 nm and this range has 30% of total population. However, in the second one the same range only has 13% of the total population. The other samples need more data for comparison.

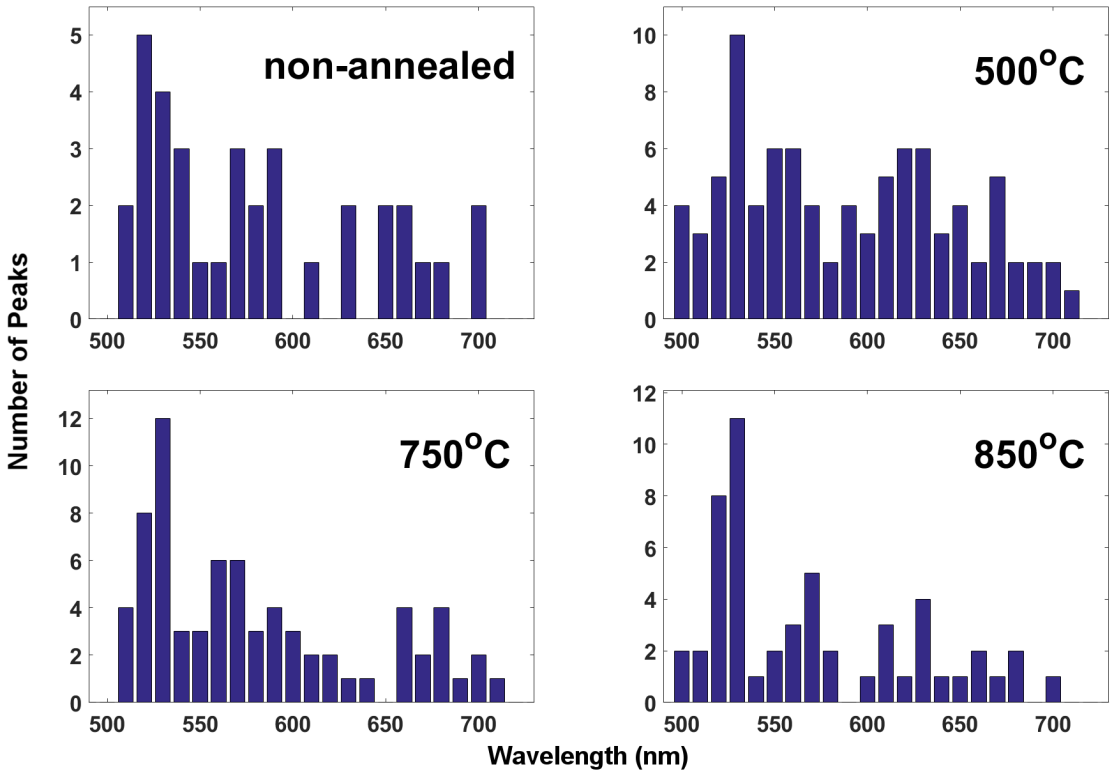

Figure 4.15. Statistics of the PL peaks from annealed and non-annealed samples.

CHAPTER 5

CONCLUSION

In this thesis the optical properties of the point defects in hBN has been investigated. We successfully created defects and showed the optical properties that reveal the emission characteristics from discrete energy levels. Our results are compatible with the literature.

In Chapter 3 we showed the DFT simulation results and found that the bandgap of monolayer hBN is about 4.52 eV. Then we made simulation of N_V defect in a 7x7 supercell and observed the formation of discrete energy levels in the bandgap.

In Chapter 4 we made Raman and PL maps to find the defects. We found the Raman shift of hBN around 1365-1366 cm^{-1} and observed sharp PL signals in visible range. The average defect size is about 0.5 μm which is limited by the magnification, NA, working distance of the objective and step-size used in the mapping process. The excitation polarization dependent measurements gave the dipole properties of the defects and we observed a dipole behaviour with 78% visibility. Theoretically, the visibility is 100% for a single dipole. The lower value of visibility can be explained by another emitter near the defect, background emission or orientation of the dipole. The power dependent measurements showed saturation behaviour at relatively low powers. This behaviour is an indication of discrete energy levels. Temperature dependence measurements gave information about the ZPL of the defects. From the PL spectrum of a defect, we found that the FWHM of the ZPL as narrow as 0.8 meV at 83 K and the peak center had a blue-shift about 6 meV from 293 to 83 K. Finally, we made a histogram of peak wavelengths. We found that most of the defects emit at wavelengths around 520-530 nm.

We are currently improving the micro-Raman/PL setup to extend its capabilities. Our next step will be constructing an HBT interferometer for auto-correlation measurements and showing the single photon emissions. Then we will add a polarizer for emission polarization measurements. Finally, we will add a time resolved PL setup for lifetime measurements.

REFERENCES

Aharonovich, I., S. Castelletto, D. Simpson, C. Su, A. Greentree, and S. Prawer (2011). Diamond-based single-photon emitters. *Reports on progress in Physics 74*(7), 076501.

Atkins, P. W. and R. S. Friedman (2011). *Molecular quantum mechanics*. Oxford university press.

Bennett, C. H. (1984). Quantum cryptography: Public key distribution and coin tossing. In *International Conference on Computer System and Signal Processing, IEEE, 1984*, pp. 175–179.

Blase, X., A. Rubio, S. G. Louie, and M. L. Cohen (1995). Quasiparticle band structure of bulk hexagonal boron nitride and related systems. *Physical review B 51*(11), 6868.

Cassabois, G., P. Valvin, and B. Gil (2016). Hexagonal boron nitride is an indirect bandgap semiconductor. *Nature Photonics*.

Choi, S., B. C. Johnson, S. Castelletto, C. Ton-That, M. R. Phillips, and I. Aharonovich (2014). Single photon emission from zno nanoparticles. *Applied Physics Letters 104*(26), 261101.

Fox, M. (2006). *Quantum optics: an introduction*, Volume 15. OUP Oxford.

Giannozzi, P., S. Baroni, N. Bonini, M. Calandra, R. Car, C. Cavazzoni, D. Ceresoli, G. L. Chiarotti, M. Cococcioni, I. Dabo, et al. (2009). Quantum espresso: a modular and open-source software project for quantum simulations of materials. *Journal of physics: Condensed matter 21*(39), 395502.

Gorbachev, R. V., I. Riaz, R. R. Nair, R. Jalil, L. Britnell, B. D. Belle, E. W. Hill, K. S. Novoselov, K. Watanabe, T. Taniguchi, et al. (2011). Hunting for monolayer boron nitride: optical and raman signatures. *Small 7*(4), 465–468.

Jackson, J. D. (1999). *Classical electrodynamics*. Wiley.

Jungwirth, N. R., B. Calderon, Y. Ji, M. G. Spencer, M. E. Flatté, and G. D. Fuchs (2016). Temperature dependence of wavelength selectable zero-phonon emission from single defects in hexagonal boron nitride. *arXiv preprint arXiv:1605.04445*.

Kiraz, A., M. Atatüre, and A. Imamoğlu (2004). Quantum-dot single-photon sources: Prospects for applications in linear optics quantum-information processing. *Physical Review A 69*(3), 032305.

Kokalj, A. (2003). Computer graphics and graphical user interfaces as tools in simulations of matter at the atomic scale. *Computational Materials Science 28*(2), 155–168.

Lienhard, B., T. Schröder, S. Mouradian, F. Dolde, T. T. Tran, I. Aharonovich, and D. R. Englund (2016). Bright and stable visible-spectrum single photon emitter in silicon carbide. *arXiv preprint arXiv:1603.05759*.

Lin, L., Y. Xu, S. Zhang, I. M. Ross, A. Ong, and D. A. Allwood (2014). Fabrication and luminescence of monolayered boron nitride quantum dots. *Small 10*(1), 60–65.

Lounis, B. and M. Orrit (2005). Single-photon sources. *Reports on Progress in Physics 68*(5), 1129.

Marder, M. P. (2010). *Condensed matter physics*. John Wiley & Sons.

Morfa, A. J., B. C. Gibson, M. Karg, T. J. Karle, A. D. Greentree, P. Mulvaney, and S. Tomljenovic-Hanic (2012). Single-photon emission and quantum characterization of zinc oxide defects. *Nano letters 12*(2), 949–954.

Ooi, N., A. Rairkar, L. Lindsley, and J. Adams (2005). Electronic structure and bonding in hexagonal boron nitride. *Journal of Physics: Condensed Matter 18*(1), 97.

Ooi, N., V. Rajan, J. Gottlieb, Y. Catherine, and J. Adams (2006). Structural properties of hexagonal boron nitride. *Modelling and Simulation in Materials Science and Engineering 14*(3), 515.

Parker Jr, J., D. Feldman, and M. Ashkin (1967). Raman scattering by silicon and germanium. *Physical Review 155*(3), 712.

Paszkowicz, W., J. Pelka, M. Knapp, T. Szyszko, and S. Podsiadlo (2002). Lattice parameters and anisotropic thermal expansion of hexagonal boron nitride in the 10–297.5 k temperature range. *Applied Physics A 75*(3), 431–435.

Santori, C., D. Fattal, and Y. Yamamoto (2010). *Single-photon devices and applications*. John Wiley & Sons.

Serrano, J., A. Bosak, R. Arenal, M. Krisch, K. Watanabe, T. Taniguchi, H. Kanda, A. Rubio, and L. Wirtz (2007). Vibrational properties of hexagonal boron nitride: inelastic x-ray scattering and ab initio calculations. *Physical review letters 98*(9), 095503.

Shi, Y., C. Hamsen, X. Jia, K. K. Kim, A. Reina, M. Hofmann, A. L. Hsu, K. Zhang, H. Li, Z.-Y. Juang, et al. (2010). Synthesis of few-layer hexagonal boron nitride thin film by chemical vapor deposition. *Nano letters 10*(10), 4134–4139.

Solozhenko, V., A. Lazarenko, J.-P. Petitet, and A. Kanaev (2001). Bandgap energy of graphite-like hexagonal boron nitride. *Journal of Physics and Chemistry of Solids 62*(7), 1331–1334.

Topsakal, M., E. Aktürk, and S. Ciraci (2009). First-principles study of two-and one-dimensional honeycomb structures of boron nitride. *Physical Review B 79*(11), 115442.

Tran, T. T. et al. (2016a). Quantum emission from hexagonal boron nitride monolayers. *Nature nanotechnology 11*(1), 37–41.

Tran, T. T. et al. (2016b). Robust multicolor single photon emission from point defects in hexagonal boron nitride. *arXiv preprint arXiv:1603.09608*.

Warner, J. H., M. H. Rümmeli, A. Bachmatiuk, and B. Büchner (2010). Atomic resolution imaging and topography of boron nitride sheets produced by chemical exfoliation. *ACS nano 4*(3), 1299–1304.

Watanabe, K., T. Taniguchi, and H. Kanda (2004). Direct-bandgap properties and evidence for ultraviolet lasing of hexagonal boron nitride single crystal. *Nature materials 3*(6), 404–409.

Zunger, A., A. Katzir, and A. Halperin (1976). Optical properties of hexagonal boron nitride. *Physical Review B 13*(12), 5560.

APPENDIX A

MATLAB PROGRAM TO GENERATE RAMAN/PL MAPS

We use the TriVista software for controlling the micro Raman/PL setup and data acquisition. This program saves the data files in csv (comma-separated values) and tvf (TriVista file) formats. Csv is a widely used format which is easy to work with.

We developed a Matlab program named as tvf2map. All Raman and PL maps in this thesis were generated by this program. The sample was scanned point by point and the spectrum of each point was recorded by the TriVista program. First version of tvf2map was just a simple Matlab code using csv files to generate Raman maps. We know that the Raman shift of Si is 520 cm^{-1} and hBN is around 1365 cm^{-1}. Therefore we just manually filtered the intensity values for those wavenumbers to generate Raman maps.

We opened a tvf file by a text editor and realized that it is an xml file. The tvf file contains extra data, such as wavelength of the laser, grating density, exposure time etc., as well as spectrum data. These extra data are very useful for analysing the data automatically. We use the xml2struct utility in Matlab to convert xml file into a Matlab structure. The second version of tvf2map was using the tvf files.

Up to this point the program was enough for Raman maps because we had already known the wavenumbers to filter; on the other hand, in PL maps we didn't know what the wavelengths of the PL emissions were. To find the PL peaks we used the findpeaks command and scanned all the spectra in a map. The wavelengths of the PL peaks were added to a list. The findpeaks command found hundreds of peaks because of the noise, therefore we applied a threshold to eliminate noise peaks. Also we added graphical user interface (GUI) to select a wavelength from the list. To sum up, the third version of the tvf2map had GUI, and it automatically find PL peaks and listed them in a clickable menu.

In the fourth version, we added extra capabilities like superimposing multiple maps, finding the size of defects by Gaussian fit, selectable threshold levels etc. Additionally, we made several improvements to the code and GUI. This is the final version of tvf2map and the GUI and code is given in the following pages.

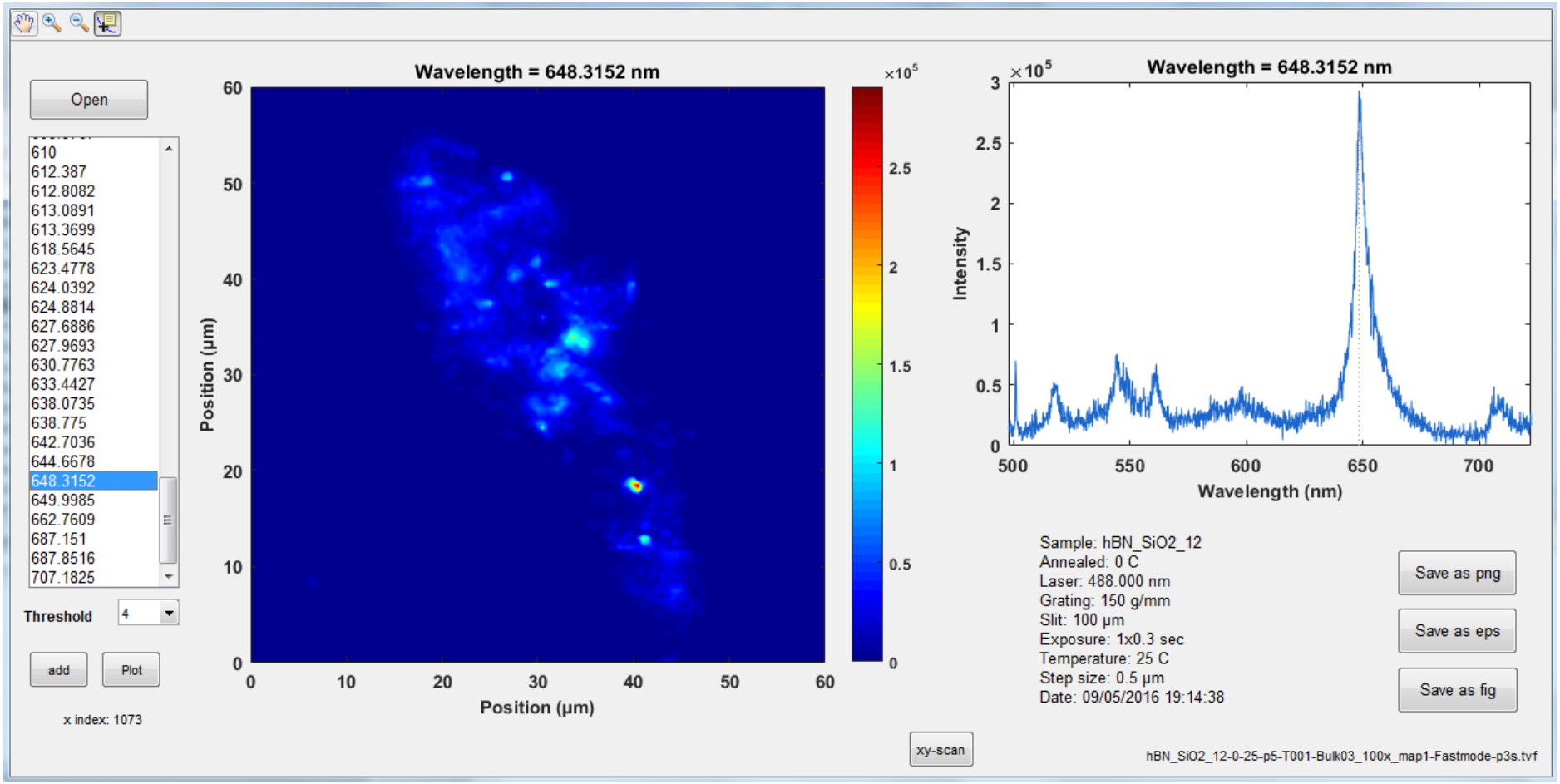

Figure A1. Graphical user interface of tvf2map

```
%{
Author: Volkan FIRAT
Mail: e122720@gmail.com
Date: 24-08-2016
Version: 4e
%}

%{  TriVista software saves the spectrum and map data in xml format with tvf extension.
       This program opens the tvf maps, extract settings and experimental data, and plot
       the maps. It has several functionalities, such as automatically finding PL
       peaks, superimposing multiple maps, determining the size of the emitter by
       Gaussian fit, saving the maps as fig, png, eps files.
%}

function varargout = tvf2map(varargin)
% Begin initialization code - DO NOT EDIT
gui_Singleton = 1;
gui_State = struct('gui_Name',       mfilename, ...
                   'gui_Singleton',  gui_Singleton, ...
                   'gui_OpeningFcn', @tvf2map_OpeningFcn, ...
                   'gui_OutputFcn',  @tvf2map_OutputFcn, ...
                   'gui_LayoutFcn',  [] , ...
                   'gui_Callback',   []);
if nargin && ischar(varargin{1})
    gui_State.gui_Callback = str2func(varargin{1});
end

if nargout
    [varargout{1:nargout}] = gui_mainfcn(gui_State, varargin{:});
else
    gui_mainfcn(gui_State, varargin{:});
end
% End initialization code - DO NOT EDIT


% --- Executes just before tvf2map is made visible.
function tvf2map_OpeningFcn(hObject, eventdata, handles, varargin)
% variables and parameters
handles.grid_NxN=1;
handles.data_x=[];
handles.data_y=[];
handles.peaks_list_index=[];
handles.isRaman=0;
handles.stepSize=1;
handles.PathName='';
handles.FileName='';
handles.wl_text='nofile';
handles.wl_added=[];
handles.wl_added_x=[];
handles.wl_index=10;
handles.max_peak_index=10;
handles.currentPath='';
handles.numOfPoints=1;
% demo map and plot
axes(handles.map_figure);
contourf(magic(7),50,'LineStyle','none');
datacursormode on;
colorbar;
axes(handles.spectrum_plot);
plot(magic(7));
% Choose default command line output for tvf2map
handles.output = hObject;

% Update handles structure
guidata(hObject, handles);


% --- Outputs from this function are returned to the command line.
function varargout = tvf2map_OutputFcn(hObject, eventdata, handles)
varargout{1} = handles.output;


% --- Executes on selection change in listbox1.
function listbox1_Callback(hObject, eventdata, handles)
contents = cellstr(get(hObject,'String'));
wavelength=contents{get(hObject,'Value')};
index_selected = get(handles.listbox1,'Value');
```

```
wavelength_index=handles.peaks_list_index(index_selected);
handles.wl_index=wavelength_index; % index of the wavelength selected in the list

set(handles.indexText,'String',['x index: ',num2str(wavelength_index)]);

% populate the grid for the chosen wavelength
grid_NxN=handles.grid_NxN;
handles.data_grid=zeros(grid_NxN,grid_NxN);

for row=1:grid_NxN
    for column=1:grid_NxN
        y_row=(row-1)*grid_NxN+column;
        handles.data_grid(row,column)=handles.data_y(y_row,wavelength_index);
    end
end


% plot the grid as map
axes(handles.map_figure);
xPos=(0:(grid_NxN-1))*handles.stepSize;
yPos=xPos;
contourf(xPos,yPos,handles.data_grid,100,'LineStyle','none');
colorbar;
colormap jet;
ax=gca;
ax.FontWeight='bold';
ax.FontSize=11;
wl_text=num2str(handles.data_x(wavelength_index));
handles.wl_text=wl_text;
if handles.isRaman == 1
    title(['Raman Shift = ' wl_text ' cm^{-1}']);
else
    title(['Wavelength = ' wl_text ' nm']);
end
xlabel('Position (µm)','FontWeight','bold','FontSize',11);
ylabel('Position (µm)','FontWeight','bold','FontSize',11);
axis('square');
% find row and column index of brightest peak in the current map
[r,column]=max(max(handles.data_grid));
[r,row]=max(max(transpose(handles.data_grid)));

% data_y index of the above peak
max_peak_index = (row-1)*grid_NxN+column;
handles.max_peak_index=max_peak_index;

% plot the spectrum
axes(handles.spectrum_plot);

wl_show=str2double(wavelength);
y_max=max(handles.data_y(max_peak_index,:));
y_min=min(handles.data_y(max_peak_index,:));
plot([wl_show,wl_show],[y_min,y_max],':','Color',[0.9,0.5,0.1]);

hold on;

max_peak_y=handles.data_y(max_peak_index,:);
plot(handles.data_x,max_peak_y,'Color',[0.1,0.4,0.8]);
xlim([handles.data_x(1),handles.data_x(end)]);
ax=gca;
ax.FontWeight='bold';
ax.FontSize=11;

if handles.isRaman == 1
    title(['Raman Shift = ' wl_text ' cm^{-1}']);
    xlabel('Raman Shift (cm^{-1})','FontWeight','bold','FontSize',11);
    ylabel('Intensity','FontWeight','bold','FontSize',11);
else
    title(['Wavelength = ' wl_text ' nm']);
    xlabel('Wavelength (nm)','FontWeight','bold','FontSize',11);
    ylabel('Intensity','FontWeight','bold','FontSize',11);
end

hold off
guidata(hObject,handles);
```

```
% --- Executes during object creation, after setting all properties.
function listbox1_CreateFcn(hObject, eventdata, handles)
if ispc && isequal(get(hObject,'BackgroundColor'),
get(0,'defaultUicontrolBackgroundColor'))
    set(hObject,'BackgroundColor','white');
end


% --- Executes on button press in openButton.
function openButton_Callback(hObject, eventdata, handles)

[FileName,PathName] = uigetfile('*.tvf','Select a TriVista map
file',handles.currentPath);

if FileName~=0
    set(handles.listbox1,'Value',1);
    set(handles.listbox1,'String','loading...');
    pause(0.1);
    FileAddress=[PathName,FileName];
    handles.FileName=FileName;
    handles.PathName=PathName;
    handles.currentPath=PathName;
    set(handles.fileText,'String',FileName);


    xml2map=xml2struct(FileAddress); % create struct from xml file


    % get data from imported file
    Grating=xml2map(2).Children(2).Children(2).Children(4).Attributes(3).Value;
    Slit=xml2map(2).Children(2).Children(2).Children(4).Attributes(8).Value;
    %CCD_Temperature=xml2map(2).Children(2).Children(2).Children(6).Attributes(7).Value;
    Exposure=xml2map(2).Children(2).Children(2).Children(6).Attributes(9).Value;

NumOfAccumulation=xml2map(2).Children(2).Children(2).Children(6).Attributes(11).Value;

Laser=xml2map(2).Children(8).Children(2).Children(8).Children(2).Attributes(3).Value;
    Date=xml2map(2).Attributes(1).Value;

    % get number of points in the map and create a grid to plot

handles.numOfPoints=str2double(xml2map(2).Children(8).Children(2).Children(12).Attribute
s.Value);
    handles.grid_NxN=sqrt(handles.numOfPoints);

    file_info=textscan(FileName,'%q','Delimiter','-');
    sample_name=file_info{1,1}{1,1};
    annealed=file_info{1,1}{2,1};
    temperature=file_info{1,1}{3,1};
    step_size=file_info{1,1}{4,1};

    if strcmp(step_size(1),'p')
        step_size=['0.',step_size(2:end)];
    end

    if isnan(str2double(step_size)) == 0
        handles.stepSize=str2double(step_size);
    else
        step_size='UNKNOWN';
    end

    if strcmp(temperature(1),'m')
        temperature=['-',temperature(2:end)];
    end

    % get x data. Note that the first element is not a data point, it is removed

raw_x=xml2map(2).Children(8).Children(2).Children(8).Children(2).Attributes(6).Value;
    data_x1=cell2mat(textscan(raw_x,'%f','Delimiter','|'));
    handles.data_x=data_x1(2:end);
    clear raw_x data_x1; % you don't need them anymore
```

```
  % determine the measurement is Raman or PL
    %Raman unit is 'relWavenumber', PL unit is 'nanometer' in tvf files

RamanOrPL=xml2map(2).Children(8).Children(2).Children(8).Children(2).Attributes(1).Value
;
    isRaman=strcmp(RamanOrPL,'relWavenumber');
    handles.isRaman=isRaman;
    % TriVista files always contain wavelength. Convert it to Raman shift if
    % it is a Raman measurement
    if isRaman == 1
        Lambda0=str2double(Laser);
        handles.data_x=(1/Lambda0-1./handles.data_x)*1e7;
    end

    % create a matrix for intensities.
    % each row contains intesities of the corresponding map point
    handles.data_y=zeros(handles.numOfPoints,1600);

    for n=1:handles.numOfPoints

raw_y=xml2map(2).Children(8).Children(2).Children(14).Children(2*n).Children.Data;
        handles.data_y(n,:)=cell2mat(textscan(raw_y,'%f','Delimiter',';'));
        % remove noise in every row
        noise=min(handles.data_y(n,:));
        handles.data_y(n,:)=handles.data_y(n,:)-noise;
    end

    clear raw_y xml2map; % you don't need them anymore.

   info_text={
            ['Sample: ' sample_name]
            ['Annealed: ' annealed ' C']
            ['Laser: ' Laser ' nm']
            ['Grating: ' Grating]
            ['Slit: ' Slit ' µm']
            ['Exposure: ' NumOfAccumulation 'x' Exposure ' sec']
            ['Temperature: ' temperature ' C']
            ['Step size: ' step_size ' µm']
            ['Date: ' Date]
            %['CCD Temp.: ' CCD_Temperature ' C']
            };

    set(handles.infoText,'String',info_text);
    set(handles.listbox1,'String','select a treshold !');
end
guidata(hObject,handles);



% --- Executes on button press in pushbutton2.
% save the map as fig file
function pushbutton2_Callback(hObject, eventdata, handles)
PathName=handles.PathName;
FileName=handles.FileName;
FigName=[PathName,FileName(1:end-4)];
set(gcf,'PaperPositionMode','auto');
savefig(FigName);
guidata(hObject,handles);



% --- Executes on button press in pushbutton3.
% save the map as png file
function pushbutton3_Callback(hObject, eventdata, handles)
wl_text=handles.wl_text;
wl_temp=textscan(wl_text,'%q','Delimiter','.');
wl_name=[wl_temp{1,1}{1,1},'p',wl_temp{1,1}{2,1}];
PathName=handles.PathName;
FileName=handles.FileName;
FigureName=[PathName,FileName(1:end-4),'_',wl_name];
set(gcf,'PaperPositionMode','auto');
print(FigureName, '-dpng','-r0');
guidata(hObject,handles);
```

```
% --- Executes on button press in addButton.
function addButton_Callback(hObject, eventdata, handles)
handles.wl_added=[handles.wl_added,handles.max_peak_index];
handles.wl_added_x=[handles.wl_added_x,handles.wl_index];
set(handles.indexText,'String',['y index: ',num2str(handles.wl_added)]);
guidata(hObject,handles);

% --- Executes on button press in plotButton.
function plotButton_Callback(hObject, eventdata, handles)

figure('Color',[1,1,1],'Position',[20,100,1300,450]);

wl_sorted=sort(handles.wl_added);
wl_unique=unique(wl_sorted);

defect_x=zeros(numel(wl_unique));
defect_y=zeros(numel(wl_unique));

RGB=[0.1 0.3 0.7;
    0.6 0.6 0.2;
    0.9 0.1 0.2;
    0.1 0.6 0.4;
    0.9 0.1 0.8;
    0.5 0.2 0.7;
    0.1 0.6 0.6;
    0.6 0.3 0.2;
    0.2 0.7 0.3;
    0.2 0.5 0.8;
    0.9 0.4 0.0;
    0.4 0.8 0.1;
    0.1 0.3 0.7;
    0.6 0.6 0.2;
    0.9 0.1 0.2;
    0.1 0.6 0.4;
    0.9 0.1 0.8;
    0.5 0.2 0.7;
    0.1 0.6 0.6;
    0.6 0.3 0.2;
    0.2 0.7 0.3;
    0.2 0.5 0.8;
    0.9 0.4 0.0];

% spectra of selected points
subArray=[];
for nn=1:numel(wl_unique)
    subplot(numel(wl_unique),2,2*(numel(wl_unique)-nn+1));
    plot(handles.data_x,handles.data_y(wl_unique(nn),:),'Color',
[RGB(nn,1),RGB(nn,2),RGB(nn,3)],'LineWidth',1);

text(handles.data_x(end),max(handles.data_y(wl_unique(nn),:)),num2str(nn),'FontSize',14,
'FontWeight','bold','Color',[RGB(nn,1),RGB(nn,2),RGB(nn,3)]);
    axis off tight;
    if nn==1 % draw x axis for the first subplot
        ax=gca;
        ax.FontWeight='bold';
        ax.FontSize=16;
        ax.XAxis.Visible = 'on';
        xlabel('Wavelength (nm)','FontSize',16,'FontWeight','bold');
    end

    if mod(wl_unique(nn),handles.grid_NxN)==0
        defect_x(nn)=(handles.grid_NxN-1)*handles.stepSize;
        defect_y(nn)=(wl_unique(nn)/handles.grid_NxN-1)*handles.stepSize;
    else
        defect_x(nn)=(mod(wl_unique(nn),handles.grid_NxN)-1)*handles.stepSize;
        defect_y(nn)=fix(wl_unique(nn)/handles.grid_NxN)*handles.stepSize;
    end
    subArray=[subArray,(2*nn-1)];
end
```

```
% superimposing the maps of the selected points
subplot(numel(wl_unique),2,subArray);
grid_NxN=handles.grid_NxN;
data_grid=zeros(grid_NxN,grid_NxN);
for pp=1:numel(handles.wl_added_x)
    for row=1:grid_NxN
        for column=1:grid_NxN
            y_row=(row-1)*grid_NxN+column;
            y_max=max(handles.data_y(:,handles.wl_added_x(pp)));
            data_grid(row,column)=data_grid(row,column)
               +handles.data_y(y_row,handles.wl_added_x(pp))/y_max;
        end
    end
end
    % plot the grid as map
    xPos=(0:(grid_NxN-1))*handles.stepSize;
    yPos=xPos;
    contourf(xPos,yPos,data_grid,100,'LineStyle','none');
    colorbar;
    colormap jet;
    ax=gca;
%     ax.FontSize=16;
%     ax.FontWeight='bold';
    ax.XAxis.Visible='off';
    ax.YAxis.Visible='off';
    %xlabel('Position (µm)','FontSize',11,'FontWeight','bold');
    %ylabel('Position (µm)','FontSize',11,'FontWeight','bold');
    axis('square');

hold on;

% mark selected points on the map
for mm=1:numel(wl_unique)

text(defect_x(mm),defect_y(mm),num2str(mm),'Color','k','FontSize',14,'FontWeight','bold'
);
end
hold off;

set(handles.indexText,'String',['y index: ',num2str(wl_sorted)]);
handles.wl_added=[];
handles.wl_added_x=[];

guidata(hObject,handles);


% --- Executes on button press in epsButton.
% save as eps file
function epsButton_Callback(hObject, eventdata, handles)

wl_text=handles.wl_text;
wl_temp=textscan(wl_text,'%q','Delimiter','.');
wl_name=[wl_temp{1,1}{1,1},'p',wl_temp{1,1}{2,1}];
PathName=handles.PathName;
FileName=handles.FileName;
FigureName=[PathName,FileName(1:end-4),'_',wl_name];
set(gcf,'PaperPositionMode','auto');
print(FigureName, '-depsc');

guidata(hObject,handles);


% --- Executes on selection change in treshMenu.
% treshold menu
function treshMenu_Callback(hObject, eventdata, handles)
contents = cellstr(get(hObject,'String'));
tresholdValue=contents{get(hObject,'Value')};

set(handles.listbox1,'Value',1);
set(handles.listbox1,'String','wait ...');
pause(0.1);
```

```
 %Low treshold finds more peaks but not good for maps that have high background emission
and high noise/signal ratio
    PeakTreshold=(max(max(handles.data_y)))/str2double(tresholdValue);

    % peaks_index is a zero matrix. it will be used to create peaks menu.
    % zero means there is no peak, 1 means there is a peak.
    peaks_index=zeros(1,1600);
    for m=1:handles.numOfPoints

[pks,locs,widths,proms]=findpeaks(handles.data_y(m,:),1:1600,'MinPeakProminence',PeakTre
shold);
        for p=1:numel(locs)
            peaks_index(locs(p))=1; % it finds a peak above the treshold and
                                    % locate it in the peaks_index
        end
    end

    % eliminate fake peaks

    for nl=numel(peaks_index):-1:2
        if peaks_index(nl)~=0 && peaks_index(nl-1)~=0
            peaks_index(nl-1)=peaks_index(nl-1)+peaks_index(nl);
            peaks_index(nl)=0;
        end
    end

    for mm=1:numel(peaks_index)
        if peaks_index(mm)>1
            D=ones(handles.numOfPoints,peaks_index(mm));
            for km=mm:(mm+peaks_index(mm)-1)
                D(:,km-mm+1)=handles.data_y(:,km);
            end
            [r,column]=max(max(D));
            for kk=mm:(mm+peaks_index(mm)-1)
                peaks_index(kk)=0;
            end
            peaks_index(mm+column-1)=1;
        end
    end


    peaks_list={}; % contains the wavelength/RamanShift of the peaks.
    peaks_list_index=[];
    for r=1:1600
        if peaks_index(r) == 1 % determine the index of the peak
            peaks_list=[peaks_list,num2str(handles.data_x(r))]; % determine the value of
the peak
            % add it to peaks_list
            peaks_list_index=[peaks_list_index,r];
        end
    end

    handles.peaks_list_index=peaks_list_index;
    set(handles.listbox1,'String',peaks_list);
    guidata(hObject,handles);

% --- Executes during object creation, after setting all properties.
function treshMenu_CreateFcn(hObject, eventdata, handles)
if ispc && isequal(get(hObject,'BackgroundColor'),
get(0,'defaultUicontrolBackgroundColor'))
    set(hObject,'BackgroundColor','white');
end
```

```
% --- Executes on button press in xyScan.
function xyScan_Callback(hObject, eventdata, handles)

% plot the x-y sections of the max peak in the current map
if mod(handles.max_peak_index ,handles.grid_NxN)==0
        defect_x1=(handles.grid_NxN);
        defect_y1=(handles.max_peak_index/handles.grid_NxN);
    else
        defect_x1=mod(handles.max_peak_index ,handles.grid_NxN);
        defect_y1=fix(handles.max_peak_index/handles.grid_NxN)+1;
end


try
    close ScanFit
catch
end

xPos=(0:(handles.grid_NxN-1))*handles.stepSize;
scan_data=zeros(numel(xPos),3);
scan_data(:,1)=xPos;
scan_data(:,2)=handles.data_grid(defect_y1,:);
scan_data(:,3)=handles.data_grid(:,defect_x1);


% plot Gaussian fit of scan data
scan_data(:,2)=scan_data(:,2)/(max(scan_data(:,2)));
scan_data(:,3)=scan_data(:,3)/(max(scan_data(:,3)));
figure('Name','ScanFit','NumberTitle','off','Position',[20,100,1200,480]);

% x-scan
subplot(1,2,1)
plot(scan_data(:,1),scan_data(:,2),'o','LineWidth',1);
ylim([-0.1,1.2]);
axis('square');
hold on
FWHM=ScanGauss(scan_data(:,1),scan_data(:,2));
text(0.5,1.1,['FWHM=',num2str(round(FWHM,2)),'µm'],'FontSize',12);
title('x-scan (Horizantal)')
xlabel('x position (µm)','FontWeight','bold')
ylabel('Normalized Intensity')
axHorz=gca;
axHorz.FontWeight='bold';
axHorz.FontSize=12;
xlim([scan_data(1,1),scan_data(end,1)]);

% y-scan
subplot(1,2,2)
plot(scan_data(:,1),scan_data(:,3),'o','LineWidth',1);
ylim([-0.1,1.2]);
axis('square');
hold on
FWHM=ScanGauss(scan_data(:,1),scan_data(:,3));
text(0.5,1.1,['FWHM=',num2str(round(FWHM,2)),'µm'],'FontSize',12);
title('y-scan (Vertical)')
xlabel('y position (µm)','FontWeight','bold')
ylabel('Normalized Intensity')
axVert=gca;
axVert.FontWeight='bold';
axVert.FontSize=12;
xlim([scan_data(1,1),scan_data(end,1)]);
%------------------------------

% save scan data file
wl_text=handles.wl_text;
wl_temp=textscan(wl_text,'%q','Delimiter','.');
wl_name=[wl_temp{1,1}{1,1},'p',wl_temp{1,1}{2,1}];
PathName=handles.PathName;
FileName=handles.FileName;
FigureName=[PathName,FileName(1:end-4),'_',wl_name];
save([FigureName,'.mat'],'scan_data');
print(gcf,[FigureName,'_scan'], '-dpng')
guidata(hObject,handles);
```

```
% Gaussian fit of horizontal/vertical scan

function FWHM = ScanGauss(SGx,SGy)
[pksMax,locsMax,wMax,pMax] = findpeaks(SGy);
[pksMin,locsMin,wMin,pMin] = findpeaks(-SGy);
[M,I] = max(pksMax);
peak_x=locsMax(I);

if isempty(locsMin)
    peak_xStart=1;
    peak_xEnd=numel(SGx);
elseif numel(locsMin)<I
    peak_xStart=locsMin(I-1);
    peak_xEnd=numel(SGx);
else
    peak_xStart=locsMin(I);
    peak_xEnd=locsMin(I);
end

if peak_xStart > peak_x
    if I == 1
        peak_xStart=1;
    else
        peak_xStart = locsMin(I-1);
    end
end
if peak_xEnd < peak_x
    if I == numel(locsMin)
        peak_xEnd=numel(SGx);
    else
        peak_xEnd = locsMin(I+1);
    end
end

if SGy(peak_xStart) < SGy(peak_xEnd)
    yshift=SGy(peak_xStart);
else
    yshift=SGy(peak_xEnd);
end

xdata=SGx(peak_xStart:peak_xEnd);
ydata=SGy(peak_xStart:peak_xEnd);

fun = @(x,xdata) x(3)./x(2).*exp(-(xdata-x(1)).^2./(2*x(2).^2))+x(4);

peak_center=SGx(locsMax(I));
Sigma=wMax(I)*(SGx(2)-SGx(1))/2.4;
area=2.4*Sigma*pksMax(I);
x0=[peak_center,Sigma,area,yshift]; % initial guesses
x = lsqcurvefit(fun,x0,xdata,ydata);
FWHM=2.3548*x(2);
xfun=linspace(SGx(1),SGx(end),1000);
plot(xfun,fun(x,xfun),'LineWidth',2)
```